



**HAL**  
open science

## Diverse Origins of Gases From Mud Volcanoes and Seeps in Tectonically Fragmented Terrane

Yueh-ting Lin, Douglas Rumble, Edward Young, Jabrane Labidi, Tzu-hsuan Tu, Jhen-nien Chen, Thomas Pape, Gerhard Bohrmann, Saulwood Lin, Li-hung Lin, et al.

► **To cite this version:**

Yueh-ting Lin, Douglas Rumble, Edward Young, Jabrane Labidi, Tzu-hsuan Tu, et al.. Diverse Origins of Gases From Mud Volcanoes and Seeps in Tectonically Fragmented Terrane. *Geochemistry, Geophysics, Geosystems*, 2023, 24 (10), pp.e2022GC010791. 10.1029/2022GC010791 . hal-04273824

**HAL Id: hal-04273824**

**<https://hal.science/hal-04273824>**

Submitted on 7 Nov 2023

**HAL** is a multi-disciplinary open access archive for the deposit and dissemination of scientific research documents, whether they are published or not. The documents may come from teaching and research institutions in France or abroad, or from public or private research centers.

L'archive ouverte pluridisciplinaire **HAL**, est destinée au dépôt et à la diffusion de documents scientifiques de niveau recherche, publiés ou non, émanant des établissements d'enseignement et de recherche français ou étrangers, des laboratoires publics ou privés.

1 Diverse origins of gases from mud volcanoes and seeps in tectonically fragmented  
2 terrane

3

4

5 Yueh-Ting Lin<sup>1</sup>, Douglas Rumble<sup>2</sup>, Edward D. Young<sup>3</sup>, Jabrane Labidi<sup>3,4</sup>, Tzu-Hsuan  
6 Tu<sup>1,5</sup>, Jhen-Nien Chen<sup>1</sup>, Thomas Pape<sup>6</sup>, Gerhard Bohrmann<sup>6</sup>, Saulwood Lin<sup>7</sup>,  
7 Li-Hung Lin<sup>1,8\*</sup>, and Pei-Ling Wang<sup>7,8\*</sup>

8

9

10

11 <sup>1</sup>Department of Geosciences, National Taiwan University, Taipei 106, Taiwan

12 <sup>2</sup>Geophysical Laboratory, Carnegie Institution for Science, Washington DC 20015,  
13 USA

14 <sup>3</sup>Department of Earth, Planetary and Space Sciences, University of California Los  
15 Angeles, Los Angeles, CA 90095, USA

16 <sup>4</sup>Université de Paris Cité, Institut de Physique du Globe de Paris, CNRS, F-75005  
17 Paris, France

18 <sup>5</sup>Department of Oceanography, National Sun Yat-sen University, Kaohsiung 804,  
19 Taiwan

20 <sup>6</sup>MARUM – Center for Marine Environmental Sciences and Faculty of Geosciences,  
21 University of Bremen, 28359 Bremen, Germany

22 <sup>7</sup>Institute of Oceanography, National Taiwan University, Taipei 106, Taiwan

23 <sup>8</sup>Research Center for Future Earth, National Taiwan University, Taipei 106, Taiwan

24

25

26

27 \*Correspondence at:

28 Li-Hung Lin

29 Department of Geosciences, National Taiwan University, Taipei 106, Taiwan

30 Email: [lhlin@ntu.edu.tw](mailto:lhlin@ntu.edu.tw)

31

32 and

33

34 Pei-Ling Wang

35 Institute of Oceanography, National Taiwan University, Taipei 106, Taiwan

36 Email: [plwang@ntu.edu.tw](mailto:plwang@ntu.edu.tw)

37

38

39 *Key point:*

- 40 ● Mud volcanoes and gas seeps provide a rapid access to probing subsurface fluid
- 41 characteristics in tectonically active regions.
- 42 ● Thermogenic methane constitutes a major component of hydrocarbons and
- 43 forms at temperatures of 99-260°C.
- 44 ● A wide spectrum of geochemical characteristics indicates diverse formation
- 45 mechanisms and conditions that constrain gas and water origins.

46

47 *Abstract*

48 Identification of methane origins remains a challenging work as current  
49 diagnostic signals are often not sufficient to resolve individual formation and  
50 post-formation processes. To address such a knowledge gap in a tectonically active  
51 and fragmented terrain, samples from mud volcanoes, gas seeps, and springs  
52 distributed along structural features onshore and offshore of Taiwan were analyzed  
53 for their isotopic compositions of methane, nitrogen, helium, dissolved inorganic  
54 carbon, CO<sub>2</sub>, and water. Our analyses yielded  $\Delta^{13}\text{CH}_3\text{D}$  and  $\Delta^{12}\text{CH}_2\text{D}_2$  values ranging  
55 between +1.9‰ and +7.8‰, and between +3.0‰ and +19.9‰, respectively. A  
56 portion of the samples were characterized by values that represent the thermodynamic  
57 equilibrium at temperatures of 99–260°C. These temperature estimates, together with  
58 the bulk isotopic compositions and local geothermal gradients (25-30°C/km), suggest  
59 that methane was formed by thermal maturation of organic matter at depths of 2 to 9  
60 km below the land surface and channeled upward along faults. Other samples were  
61 found to deviate from equilibrium by varying degrees. Considering the geological  
62 background, helium isotopic ratios, and nitrogen isotopologue compositions, and  
63 methanogens detected at some sites, these gases are either abiotic in origin or a  
64 mixture of microbial and thermogenic sources. Regardless of whether the equilibrium  
65 of methane isotopologues was reached, few sites hosted by sedimentary formations  
66 were characterized by mantle-like helium signatures, indicating decoupled origins  
67 and potential degassing of helium from the relic igneous source. Overall, these results  
68 suggest the extraction of methane and other gases from multiple depths from strata  
69 fragmented by fault displacement in an active orogenic belt.

70

71 *Plain Language Summary*

72 Mud volcanoes and gas seeps are distributed primarily in active tectonic regimes

73 and represent the surface expression of subsurface fracture networks. They provide  
74 rapid access to probing subsurface characteristics for the generations of methane,  
75 other gases, and water. Identifying the exact mechanisms of methane formation  
76 remains a challenging work due to the lack of diagnostic signals with sufficient  
77 resolving power. This study employed a wide range of isotopic tools to constrain the  
78 origins of gases and water from mud volcanoes and seeps in Taiwan, where dual  
79 subductions and associated arc-continent collision between the Philippine Sea and  
80 Eurasian plates have enabled the plumbing of gases and water in accordance with  
81 structure development and stratum deformation. Our results reveal a spectrum of  
82 geochemical characteristics that point to diverse formation mechanisms and  
83 conditions. In particular, deeply sourced thermogenic methane (from depths of 2 to 9  
84 km) appears to constitute a major gas component at most sites, and is mixed by  
85 various degrees with abiotic methane pertinent to igneous bodies emplaced during  
86 subduction/collision, or microbial methane generated at shallow depths. Overall, the  
87 results address the temporal and spatial variations in gas origins prone to terrain  
88 fragmentation and dynamic structural control associated with mountain building.

89

90 *Keywords:*

91 methane isotopologue, helium isotope, mud volcano, seep, active tectonic regime

92 1. Introduction

93 Methane is the main gas component associated with petroleum and coal  
94 systems (Lundegard et al., 2000). Three major mechanisms have been suggested for  
95 its formation, including biological production from CO<sub>2</sub> and methylated compounds,  
96 stepwise thermal degradation of complex organic matters, and to a lesser extent, the  
97 Fischer-Tropsch Type reaction catalyzed by metals or sulfide minerals (Kietäväinen  
98 & Purkamo, 2015; Schoell, 1988; Stolper et al., 2014). Identifying the exact  
99 mechanisms and quantifying their fluxes from individual sources would greatly  
100 enhance our understanding of carbon cycling between reservoirs and their impact on  
101 future climate.

102 Mud volcanoes and seeps represent the surface expression of subsurface fracture  
103 networks and are considered to be an effective channel of methane emission (Kopf,  
104 2003; Etiope, 2009). Gases (predominantly hydrocarbons), water, and unconsolidated  
105 sediments originating from deep environments migrate upward due to gravitational  
106 instability and overpressurization driven by rapid burial and fault displacement  
107 (Carson & Sreaton, 1998), facilitating the minimum alteration of gas during channel  
108 transport, and the direct methane emissions into the atmosphere or seawater.  
109 Therefore, the geochemical characteristics of methane (e.g., abundance and isotopic  
110 composition) could potentially serve as an indicator of methane formation conditions,  
111 and the connectivity and extent of fractures in the crustal plumbing system (Mazzini  
112 & Etiope, 2017; Milkov & Etiope, 2018).

113 Methane isotopic compositions (<sup>13</sup>C/<sup>12</sup>C and <sup>2</sup>H/<sup>1</sup>H) and abundance ratios as  
114 compared to higher hydrocarbons (C<sub>1</sub>/C<sub>2</sub><sup>+</sup>) are conventionally used to characterize  
115 methane origins (e.g., Bernard et al., 1977; Whiticar, 1999). The principle stems from  
116 experimental and field observations that constrain various degrees of isotopic  
117 fractionations and abundance ratios for different methane-formation mechanisms  
118 (Milkov and Etiope, 2018). These fingerprints are not unequivocal, as they are subject  
119 to further alteration caused by secondary processes, such as mixing, migration, and  
120 microbial oxidation (e.g., Bernard et al., 1977; Whiticar, 1999). The advancement of  
121 mass spectrometric techniques has enabled the measurement of two doubly  
122 substituted isotopologues (<sup>13</sup>CH<sub>3</sub>D and <sup>12</sup>CH<sub>2</sub>D<sub>2</sub>) at high precision (Young et al.,  
123 2016). The isotopologue approach provides a direct means to assess whether the  
124 methane has reached isotopic equilibrium (with coherent temperature estimates from

125 two thermometers), overcoming the potential bias derived from the abundance of  
126 single doubly substituted isotopologue quantified by either mass or optic  
127 spectroscopy (Douglas et al., 2017; Ono et al., 2014; Young et al., 2016). Furthermore,  
128 the approach adds two additional constraints to conventional mixing models based on  
129 mass conservation, thereby facilitating coherent reservoir or process mixing models  
130 among different isotopic signals and better identification of end components. Finally,  
131 gas origins could best be resolved with additional isotopic fingerprints of the  
132 constituent gases. While helium isotope ratios are conventionally exploited to  
133 differentiate mantle from crust and atmospheric sources (Poreda & Craig, 1989), the  
134 abundances of rare nitrogen isotopologues emerge as a sensitive indicator to track the  
135 cycling of air-derived nitrogen that could be falsely identified as the mantle nitrogen  
136 using the bulk nitrogen isotopic compositions (Labidi and Young, 2022). The  
137 approaches arise from the observation that mantle derived  $^{15}\text{N}^{15}\text{N}$  abundances (from  
138 mid-ocean ridges and plumes) are consistent with the stochastic distribution for the  
139 intramolecular equilibrium, and are greatly distinctive from atmospheric nitrogen  
140 (Labidi et al., 2020). These results combined with bulk nitrogen isotopic  
141 compositions and noble gas ratios enable to trace nitrogen cycling associated with  
142 subduction and hydrothermal circulation potentially impacted by air contamination,  
143 as well as to identify the primordial mantle (Labidi et al., 2020 and 2021; Labidi and  
144 Young, 2022). As terranes associated with subduction systems are fragmented by  
145 faulting and magmatism, gases that originate from multiple sources likely have  
146 distinctive combined isotopic patterns. The integration of multiple isotopic  
147 fingerprints (bulk and isotopologue) for specific geological occurrences offers  
148 insights into gas formation, mixing, and alteration that have rarely been explored.

149 This study aims to determine the origins of methane from mud volcanoes and  
150 seeps onshore and offshore Taiwan by combining the abundances of rare methane and  
151 nitrogen isotopologues, and bulk isotopic compositions of helium, methane,  
152 dissolved inorganic carbon (DIC),  $\text{CO}_2$ , and water. The study materials were chosen  
153 to take advantage of Taiwan's unique tectonic setting, at the intersection of dual  
154 subduction systems between the Eurasian and Philippine Sea plates (Lallemant,  
155 2016). Mud volcanoes/seeps are associated with different structural features in  
156 different geological units, providing ideal opportunities to probe gas reservoirs in  
157 fragmented subsurface environments. These isotopic results were integrated with

158 geological characteristics to address mechanisms and potential depths of methane  
159 formation, and post-formation mixing and alteration.

160

## 161 2. Site background

162 Taiwan is located in an active tectonic setting, at the boundary between the  
163 Philippine Sea plate and the Eurasian plate (Suppe, 1984; Teng & Lin, 2004). Major  
164 structures are oriented roughly northeast-southwest as a result of compression driven  
165 by the convergence and collision between the Luzon arc and the Eurasian continent.  
166 Geological units on land, from west to east, include the Coastal Plain, the Western  
167 Foothills, the Hsuehshan Range, the Central Range (Backbone Range), the  
168 Longitudinal Valley, and the Coastal Range (Teng & Lin, 2004). A developing  
169 accretionary wedge is located offshore of southwestern Taiwan and features ridges  
170 and pockmarks (bathymetric depressions often interpreted as the signature of  
171 seafloor fluid transport) that have been postulated to extend from corresponding  
172 structures on land (Figure S1; Liu et al., 1997). Seismic surveys across the transect  
173 between Taiwan and the Eurasian continent reveal two structural domains (active and  
174 passive continental margins) separated by a projected deformation front that  
175 represents the extension of the Manila Trench (Lin et al., 2008). The active margin is  
176 further composed of the Upper Slope unit to the east, where mud diapirs predominate,  
177 and the Lower Slope unit to the west, where anticlinal ridges have formed (Chen et  
178 al., 2014; Wang et al., 2022). Numerous mud volcanoes and seeps are distributed  
179 along faults or near anticlinal axes in southwestern and eastern Taiwan, and offshore  
180 southwestern Taiwan (Chao et al., 2011; Chen et al., 2017; Sun et al., 2010). Field  
181 sites investigated here are distributed near, or along structures, including the Chukou  
182 fault, Chishan fault, Gutingkeng anticline, blind structures in the Coastal Plain,  
183 Longitudinal Valley fault, volcanic complexes, and the Formosa and Four Way  
184 Closure ridges offshore southwestern Taiwan (Figure S1; Table S1). A more detailed  
185 description of the site background is given in the Supporting information.

186

## 187 3. Materials and methods

### 188 3.1 Field sampling and sample processing

189 A total of 31 gas and water samples were collected from 23 mud volcanoes, gas  
190 seeps, and boreholes (Table S1). For most samples, gases were collected directly

191 from bubbling features with the most vigorous activity. Sites AT and YSES are  
192 boreholes connected with a gas-water separator. Site GI-03 was an artisan well with  
193 vigorous bubbling, whereas site GI-01 was a pond (episodically flooded with  
194 seawater) with several bubbling features. To perform sampling at most sites, gases  
195 were drained into 50 mL gas-tight, pre-evacuated glass bottles with two stopcocks  
196 connected to a funnel. The funnel was first placed above bubbling features and filled  
197 with water. Water in the funnel was replaced gradually with the exsolved gases. The  
198 gases were used to purge the connecting tubing five times, and drained into  
199 pre-evacuated glass bottles (Figure S2). Sampling procedures were adjusted for three  
200 sites (YSES, WD, and AT). For samples from sites YSES and AT, gases discharged  
201 from the gas-water separator were directly diverted into pre-evacuated glass bottles.  
202 For samples from site WD, high erupting activities and outflowing water temperatures  
203 (63°C) prohibited direct sampling access. Therefore, mud and water flowing to the  
204 rim of the affected area were drained into serum bottles without headspace and capped  
205 with blue butyl rubber stoppers. Gases were extracted by connecting the sample  
206 bottles with pre-evacuated glass bottles. A total of five replicate bottles were collected  
207 for multiple gas analyses.

208 Offshore gas samples were collected from sediment cores drilled into  
209 gas-hydrate bearing zones at Formosa Ridge (site FR) and Four Way Closure Ridge  
210 (site FWCR) with the seafloor drill rig MARUM-MeBo200 during cruise SO266 with  
211 *R/V SONNE* (Bohrmann et al., 2023). Sediment cores dedicated to gas sampling were  
212 collected with pressure core samplers (Pape et al., 2017) and kept under in situ  
213 pressure during core retrieval. During onboard gas sampling, the pressure core was  
214 first depressurized slowly while monitoring gas pressure. Gases were collected into  
215 stainless steel cylinders when the incremental gas pressure increased abruptly (up to  
216 725 psi), an indicator of hydrate dissociation.

217 For all sites, water temperatures were measured on-site. Water samples were  
218 collected in 50 mL tubes and centrifuged at a speed of 10,000 ×g for 20 min. The  
219 supernatant was filtered through 0.22 μm pore-sized cellulose membranes and stored  
220 with no headspace at room temperature.

221

### 222 3.2 Sample analyses

223 CH<sub>4</sub>, C<sub>2</sub>H<sub>6</sub>, C<sub>3</sub>H<sub>8</sub>, and CO<sub>2</sub> concentrations were analyzed by a gas

224 chromatograph (GC; 6890N, Agilent Technologies) with a flame ionization detector,  
225 and a thermal conductivity detector in line with a Porapak Q column using helium as  
226 the carrier gas. DIC concentrations were analyzed on CO<sub>2</sub> gases exsolved from  
227 water acidified with phosphoric acid (5%) using a CO<sub>2</sub> analyzer (Aurora 1030, O.I.  
228 Analytical). The reported gas abundances were corrected for the air assuming that  
229 oxygen measured was derived from the air and the N<sub>2</sub>/O<sub>2</sub> ratio is 3.7. Since all  
230 samples were collected in 5 replicates, the sample was discarded if the air  
231 constituted the main component of the gases.

232 Carbon isotopic compositions of CH<sub>4</sub>, DIC and CO<sub>2</sub> were measured with a  
233 MAT253 isotope ratio mass spectrometer (IRMS) equipped with a GC IsoLink  
234 (Thermo Fisher Scientific) hosted at the National Taiwan University. The isotopic  
235 compositions are expressed in δ notation using the following equation:

236

$$237 \delta^{13}\text{C} = (\text{R}_{\text{sample}} / \text{R}_{\text{standard}} - 1) \times 1000\text{‰} \quad \text{eq. 1}$$

238

239 where R is <sup>13</sup>C/<sup>12</sup>C, and the standard is Vienna Pee Dee Belemnite (VPDB).

240 For noble gas analyses, gases were introduced into a preline system for  
241 purification and separation. Helium isotopic ratios (<sup>3</sup>He/<sup>4</sup>He) and neon concentrations  
242 were measured by a helium isotope mass spectrometer (Helix, Thermo Scientific) in  
243 line with a quadrupole mass spectrometer (QMS200, Pfeiffer Vacuum). Helium ratios  
244 were calibrated against the standard atmospheric helium (Mishima et al., 2018) and a  
245 standard with a <sup>3</sup>He/<sup>4</sup>He ratio 20.4 times of the atmospheric ratio (R<sub>a</sub>) provided by the  
246 University of Tokyo (Sano et al., 2008), whereas neon concentrations and He/Ne  
247 ratios were calibrated against the air. Helium isotope ratios are expressed relative to  
248 the air using the following equation:

249

$$250 \text{R/R}_a = (^3\text{He}/^4\text{He})_{\text{sample}} / (^3\text{He}/^4\text{He})_{\text{atmosphere}} \quad \text{eq.2}$$

251

252 where R and R<sub>a</sub> are the <sup>3</sup>He/<sup>4</sup>He ratios of sample and atmospheric helium,  
253 respectively.

254 Hydrogen and oxygen isotope compositions of water were measured by an  
255 Off-Axis Integrated Cavity Output Spectrometer (Los Gatos Research). The isotopic  
256 compositions are expressed in δ notation (eq. 1) with reference to VSMOW (Vienna

257 Standard Mean Ocean Water).

258 Typical analytical uncertainties were 5% for gas concentrations, 2% for DIC  
259 concentrations, 0.2‰ for  $\delta^{13}\text{C}$  values, 0.2‰ for  $\delta^{18}\text{O}_{\text{H}_2\text{O}}$  values, 1.0‰ for  $\delta^2\text{H}_{\text{H}_2\text{O}}$   
260 values, and 2% for  $^3\text{He}/^4\text{He}$ . The detection limits for gas abundances and DIC  
261 concentrations were 10 ppmv, and 0.05 mM, respectively.

262 For methane isotopologues, currents of  $^{12}\text{CH}_4^+$ ,  $^{13}\text{CH}_4^+$ ,  $^{12}\text{CH}_3\text{D}^+$ ,  $^{13}\text{CH}_3\text{D}^+$ , and  
263  $^{12}\text{CH}_2\text{D}_2^+$  were measured using the Panorama (Nu Instruments) at the University of  
264 California at Los Angeles following established protocols (Giunta et al., 2019; Young  
265 et al., 2016, 2017). The mass resolving power of the spectrometer was equal to, or  
266 greater than 40,000, allowing for the resolution of two mass-18 isotopologues,  
267  $^{13}\text{CH}_3\text{D}$  and  $^{12}\text{CH}_2\text{D}_2$ . Methane was purified using a GC equipped with two packed  
268 columns filled with 5A molecular sieve and HayeSepD porous polymer using helium  
269 as the carrier gas. Purified methane was collected, transferred, and expanded into the  
270 sample bellows connected to the mass spectrometer. In general,  $^{12}\text{CH}_3\text{D}^+ / ^{12}\text{CH}_4^+$  and  
271  $^{12}\text{CH}_2\text{D}_2 / ^{12}\text{CH}_4^+$  ratios, and  $^{13}\text{CH}_4^+ / ^{12}\text{CH}_4^+$  and  $^{13}\text{CH}_3\text{D} / ^{12}\text{CH}_4^+$  ratios were measured  
272 with more than twenty blocks of data acquisition. In each block, alternating  
273 measurements on 20 samples and 21 standards were cycled every 30 seconds. Data  
274 was further integrated over individual blocks. The bulk isotopic compositions are  
275 adopted from  $^{13}\text{CH}_4^+ / ^{12}\text{CH}_4^+$  and  $^{12}\text{CH}_3\text{D}^+ / ^{12}\text{CH}_4^+$ , and expressed in  $\delta$  notation ( $\delta^{13}\text{C}$   
276 and  $\delta^2\text{H}$  referenced to VPDB and VSMOW, respectively; eq. 1), whereas the  
277 isotopologue abundances are shown as uppercase delta values, defined as:

278

$$279 \Delta^{13}\text{CH}_3\text{D} = [ (^{13}\text{CH}_3\text{D} / ^{12}\text{CH}_4)_{\text{sample}} / (^{13}\text{CH}_3\text{D} / ^{12}\text{CH}_4)_{\text{stochastic}} - 1 ] \times 1000\text{‰} \quad \text{eq. 3}$$

$$280 \Delta^{12}\text{CH}_2\text{D}_2 = [ (^{12}\text{CH}_2\text{D}_2 / ^{12}\text{CH}_4)_{\text{sample}} / (^{12}\text{CH}_2\text{D}_2 / ^{12}\text{CH}_4)_{\text{stochastic}} - 1 ] \times 1000\text{‰} \quad \text{eq. 4}$$

281

282 where the ratio of the isotopologues under stochastic conditions was calculated using  
283 the bulk isotope composition. Typical internal uncertainties for  $\Delta^{13}\text{CH}_3\text{D}$ , and  
284  $\Delta^{12}\text{CH}_2\text{D}_2$  values were less than  $\pm 0.2\text{‰}$  and  $\pm 0.6\text{‰}$   $1\sigma$ , respectively (Young et al.,  
285 2016, 2017).

286 The equilibrium temperatures were calculated following the relationship  
287 described in Young et al. (2016 and 2017):

288

$$289 \Delta^{13}\text{CH}_3\text{D} \approx 1000 \times \ln ( 1 + 0.0355502 / T - 433.038 / T^2 + 1270210.0 / T^3 - 5.94804 \times 10^8 /$$

290  $T^4 + 1.196630 \times 10^{11}/T^5 - 9.0723 \times 10^{12}/T^6$  eq. 5

291

292  $\Delta^{12}\text{CH}_2\text{D}_2 \approx 1000 \times \ln(1 + 0.183798/T - 785.483/T^2 + 1056280.0/T^3 + 9.37307 \times$   
 293  $10^7/T^4 - 8.919480 \times 10^{10}/T^5 + 9.901730 \times 10^{12}/T^6)$  eq. 6

294

295 where T is in Kelvin.

296 Nitrogen isotopologues for five samples (sites KTL-02, WSD-01, AT, GI-01, and  
 297 GI-03) were also determined. In short, nitrogen was purified on the same preline  
 298 system as methane (Young et al., 2016). The abundances of  $^{14}\text{N}^{14}\text{N}^+$ ,  $^{14}\text{N}^{15}\text{N}^+$ , and  
 299  $^{15}\text{N}^{15}\text{N}^+$  ions were measured at a mass resolving power of approximately 50,000  
 300 (Labidi & Young, 2022). Data are expressed as  $\delta^{15}\text{N}$  (eq. 1; referenced to the air) and  
 301  $\Delta_{30}$  (Yeung et al., 2017):

302

303  $\Delta_{30} = ({}^{30}\text{R}/({}^{15}\text{R})^2 - 1) \times 1000\%$  eq. 7

304

305 where  ${}^{30}\text{R} = {}^{15}\text{N}^{15}\text{N}/{}^{14}\text{N}^{14}\text{N}$  and  ${}^{15}\text{R} = {}^{15}\text{N}/{}^{14}\text{N}$ .

306

#### 307 4. Results

308 Gas compositions and isotopic compositions are shown in Figure 1 and Table S1.  
 309 Gases in most samples were dominated by methane (>75%), with the exception of  
 310  $\text{CO}_2$ -rich (>80%) gases from sites CLS and CLP (Table S1). Minor amounts of ethane  
 311 (0.1-1.7%) and propane (0-0.4%) were observed in all samples. Bulk carbon and  
 312 hydrogen isotopic compositions of methane spanned over a wide range ( $\delta^{13}\text{C}_{\text{CH}_4}$  from  
 313 -86.9‰ to -16.7‰ and  $\delta^2\text{H}_{\text{CH}_4}$  from -206.4‰ to -78.4‰) with the majority of  $\delta^{13}\text{C}_{\text{CH}_4}$   
 314 and  $\delta^2\text{H}_{\text{CH}_4}$  values clustering between -39.3‰ and -30.7‰ and between -167.8‰ and  
 315 -138.5‰, respectively. While DIC  $\delta^{13}\text{C}$  values were from -29.5‰ to +30.6‰, DIC  
 316 concentrations varied considerably between 0.4 mM and 271.3 mM. For comparison,  
 317  $\delta^{13}\text{C}_{\text{CO}_2}$  values ranged from -24.8‰ to +20.5‰.

318 The  $\Delta^{13}\text{CH}_3\text{D}$  and  $\Delta^{12}\text{CH}_2\text{D}_2$  values ranged between +1.90‰ and +7.83‰ and  
 319 between +2.97‰ and +19.85‰, respectively (Figure 2; Table S2). Among all  
 320 samples, eight (CLP, CLS, KTL, SYNH-02, WSD-01, WD, AT, and LS) had  
 321 isotopologue abundances consistent with the thermodynamic equilibrium at  
 322 temperatures ranging from 23°C to 260°C (Table S2). Other samples were

323 characterized. by values deviating from the equilibrium by varying degrees (Figure 2).  
324 The  $\delta^{15}\text{N}$  and  $\Delta_{30}$  values ranged between -2.1‰ and +3.6‰, and between 1.8‰ and  
325 16.4‰ relative to the stochastic distribution of isotopologues, respectively (Figure S3;  
326 Table S3).

327 Helium isotopic compositions spanned from 0.1 to 5.4 Ra. Eight samples  
328 possessed  $^3\text{He}/^4\text{He}$  ratios of >1 Ra (Figure 3; Table S4). The  $\delta^2\text{H}_{\text{H}_2\text{O}}$  and  $\delta^{18}\text{O}_{\text{H}_2\text{O}}$   
329 values spanned from -52.5‰ to -1.0‰, and from -8.1‰ to +6.4‰, respectively  
330 (Figure 4a; Table S5). While eight samples from the Chukuo fault and Coastal Range  
331 fell along the local meteoric water line (LMWL; Peng et al., 2010), the others deviated  
332 from the LMWL by varying degrees.

333

## 334 5. Discussion

### 335 5.1 First order assessments on the origins of methane

336 Conventional approaches based on bulk isotopic compositions of methane and  
337  $\text{CO}_2$ , and abundance ratios were first used to interpret the origins of hydrocarbon  
338 gases for individual structural domains (e.g., Milkov, 2011; Milkov & Etiope, 2018).  
339 The principle stems from laboratory and field observations (e.g., Bernard et al., 1977;  
340 Whiticar, 1999; Milkov & Etiope, 2018) that thermogenic gases are generally  
341 characterized by relatively high  $\delta^{13}\text{C}_{\text{CH}_4}$  and  $\delta^2\text{H}_{\text{CH}_4}$  values (from -60‰ to -25‰, and  
342 -300‰ to -150‰, respectively), low  $\text{C}_1/\text{C}_2^+$  ratios (1 to 100), and low  $\delta^{13}\text{C}_{\text{CO}_2}$  values.  
343 Microbial gases possess geochemical characteristics (low  $\delta^{13}\text{C}_{\text{CH}_4}$  and  $\delta^2\text{H}_{\text{CH}_4}$  values  
344 (< -50‰ and < -150‰, respectively; Whiticar, 1999), and high  $\text{C}_1/\text{C}_2^+$  ratios (>1000;  
345 Bernard et al., 1977)) distinct from thermogenic gases by various degrees (even  
346 though the less fractionated isotopic compositions of microbial methane resemble  
347 early mature thermogenic gases). Abiotic gases may follow variable patterns  
348 partially overlapping with thermogenic gases and with a tendency toward greater  
349  $\delta^{13}\text{C}_{\text{CH}_4}$  values (Milkov & Etiope, 2018). For comparison, as  $\text{CO}_2$  derived from  
350 biodegraded oil is converted into secondary microbial methane, the residual  $\text{CO}_2$   
351 becomes progressively enriched in  $^{13}\text{C}$  (Head et al., 2003). Biodegradation also leads  
352 to an increasing  $\text{CH}_4$  fraction in the gas. Furthermore, methane oxidation (aerobic  
353 and anaerobic styles) and diffusive transport would all lead to the residue methane  
354 enriched with  $^{13}\text{C}$  and  $^2\text{H}$  by various degrees (Figure 1; Whiticar, 1999). Therefore,  
355 gas alteration and mixing can complicate possible interpretations.

356 Based on these empirical fields defined in  $\delta^{13}\text{C}$  and  $\delta^2\text{H}$  values, and  $\text{C}_1/\text{C}_2^+$  ratios,  
357 15 out of the 31 samples could be interpreted as dominantly thermogenic in origin  
358 (Figure 1; Table S1; S2). While these samples were primarily distributed along the  
359 Chukou and Chishan faults, 4 of the 15 were from the Coastal Range (sites LGH and  
360 LS), the Gutingkeng anticline (site LCW), and the Coastal Plain (site WD). For  
361 comparison, data for two boreholes from the Coastal Range (sites AT and GI) were  
362 interpreted as abiotic in origin (Figure 1). On the Bernard plot (Figure 1b), these data  
363 points fell either within the empirically defined abiotic field or the overlapping range  
364 between the thermogenic and abiotic fields (Milkov and Etiope, 2018). The  $\delta^2\text{H}_{\text{CH}_4}$   
365 values for both sites (between -79‰ and -77‰) and the  $\delta^{13}\text{C}_{\text{CH}_4}$  value for site GI were  
366 much higher than those commonly identified as thermogenic methane. This,  
367 combined with their high temperature nature, proximity to the volcanic bodies, and  
368 island arc setting suggest that methane could be abiotic (Milkov, 2011; Milkov and  
369 Etiope, 2018). Data for two marine sediments (sites FR and FWCR) were categorized  
370 as microbial in origin, whereas data points for LGH (Coastal Range), TDS (Coastal  
371 Plain), YSES (Chukou fault), and all samples from the Gutingkeng anticline fell  
372 between typical ranges of thermogenic and microbial end components (Figure 1b; see  
373 section 5.3 for the mixing model).

374 The  $\delta^{13}\text{C}_{\text{CO}_2}$  values of samples collected from the Chishan fault fell between  
375 -15.9‰ and +20.5‰ (Figure 1c; Table S1). In particular,  $\delta^{13}\text{C}$  values of  $\text{CO}_2$  and DIC  
376 for SYNH-01, and WSD -01 and -02 ranged from +8.9‰ to +20.5‰ and from  
377 +18.5‰ to +30.6‰, respectively. This, combined with the detection of active  $\text{CO}_2$   
378 reducing methanogens in the region (Cheng et al., 2012; Lin et al., 2018) suggests that  
379 the  $^{13}\text{C}$  enrichment in  $\text{CO}_2$  is catalyzed by secondary methane formation from  $\text{CO}_2$ .  
380 Secondary microbial methane is formed through the anaerobic degradation of  
381 petroleum (Head et al., 2003). As  $\text{CO}_2$  is the byproduct of petroleum degradation, its  
382 quantity is limited by the degradability of petroleum, and therefore, considered as the  
383 close system. In this regard, further methane formation would preferentially reduce  
384  $^{12}\text{CO}_2$  over  $^{13}\text{CO}_2$ , leaving the residue  $\text{CO}_2$  enriched with  $^{13}\text{C}$  and methane depleted in  
385  $^{13}\text{C}$ . The interpretation is also supported by the presence of patchy oils constantly  
386 observed in the bubbling pools or craters. To assess this process, a Rayleigh  
387 distillation model was applied assuming an initial  $\delta^{13}\text{C}_{\text{DIC}}$  value of -25‰ and a  
388 fractionation factor ( $\alpha_{\text{DIC-CH}_4}$ ) of 1.05 (Chasar et al., 2000). The calculation also

389 assumed that CO<sub>2</sub> or DIC in environments was produced primarily from the  
390 degradation of organic matter with δ<sup>13</sup>C values between -30‰ and -20‰ (Campeau  
391 et al., 2017). Since the isotopic fractionation for organic degradation is small (<1‰),  
392 the median δ<sup>13</sup>C value (-25‰) was arbitrarily chosen for modeling. The calculation  
393 suggests that in order to replicate the observed δ<sup>13</sup>C<sub>DIC</sub> value, the fraction of reaction  
394 would be 36% or the concentration of DIC consumed or methane produced would be  
395 equivalent to 57 mM. The quantity of DIC reduced or methane produced is at least  
396 one order of magnitude higher than the observed maximum methane concentration (2  
397 mM). If the fractionation factor is raised to a more extreme level of 1.08 (Summons et  
398 al., 1998), the reaction fraction would reach 54%, or the concentration of methane  
399 produced would be 34 mM. The overall results from the Rayleigh distillation  
400 modeling suggest that secondary methane formation by CO<sub>2</sub> reducing methanogens  
401 might not be solely responsible for the <sup>13</sup>C enrichment in CO<sub>2</sub> or DIC. Other microbial  
402 channels, such as acetate formation from CO<sub>2</sub> (Karakashev et al., 2006), might be  
403 involved. Alternatively, the high predicted concentration of methane could have been  
404 lost due to the depressurized degassing during transport along the fluid conduit. The  
405 temperature of methane formation for SYNH has been estimated to be up to 236°C  
406 (Figure 2; Table S2). By applying a local geothermal gradient of 25°C/km (Chi &  
407 Reed, 2008), the formation depth could range up to 9 km below the land surface. As  
408 methane ascends toward the land surface, dissolved methane would be depressurized  
409 and transformed into bubbles. The inference is supported by vigorous bubbling at  
410 SYNH during sampling.

411 The excess methane or carbon could not be accounted for by the anabolic  
412 assimilation as most substrate consumptions are often diverted to the energy yield  
413 rather than biosynthesis. For example, tests on *S. funaroxidans* cocultured with *M.*  
414 *hungate* have obtained a yield of 0.15-0.25 mole-CH<sub>4</sub>/g-dw-biomass (Scholten &  
415 Conard, 2000). If 50% of biomass is attributed to carbon, the yield would range from  
416 3.57 to 5.95 mole-CH<sub>4</sub>/mole-C-biomass. For every mole of CO<sub>2</sub> utilized, less than  
417 20% of it is diverted to biomass generation. Even with this, the predicted CO<sub>2</sub>  
418 consumption or CH<sub>4</sub> production still greatly exceeds the observed methane  
419 concentrations. In sum, the bulk isotopic compositions provide a first-order  
420 interpretation for the origin of hydrocarbons (methane in particular). While the  
421 excess methane predicted for the Chishan fault could have been accounted for by the

422 depressurization loss, the interpretation for the origins of all samples is still subject  
423 to variations caused by potential mixing with a small fraction of non-major end  
424 components.

425 The majority of  $\Delta^{13}\text{CH}_3\text{D}$  and  $\Delta^{12}\text{CH}_2\text{D}_2$  values for samples from the Chukou  
426 and Chishan faults, and the Coastal Range were distributed either on, or close to the  
427 equilibrium curve (Figure 2). The equilibrium temperatures were calculated to range  
428 from 23°C to 260°C for sites CLP, CLS, and KTL in the Chukou fault, sites WSD-01  
429 and SYNH-02 in the Chishan fault, site WD in the Coastal Plain, and sites AT and  
430 LS in the Coastal Range (Table S2). Except for sites WSD-01 and AT, samples that  
431 displayed the isotopologue equilibrium also possessed bulk isotopic compositions and  
432 abundances interpreted as the products of thermal maturation of organic matters at  
433 high temperatures. Such a pattern is comparable with the observations of large-scale  
434 continental sedimentary basins, the Southwest Ontario and the Michigan Basin, as  
435 described in Giunta et al. (2019). Although the  $\Delta^{13}\text{CH}_3\text{D}$  and  $\Delta^{12}\text{CH}_2\text{D}_2$  values for  
436 sites WSD-01 and AT yielded comparable temperature estimates, these isotopologue  
437 abundances were considered to represent either a mixture of thermogenic and  
438 microbial (for site WSD-01) sources, or abiogenic methane (for site AT) (see sections  
439 5.3 and 5.4).

440

## 441 5.2 Re-equilibration and other secondary processes for methane

442 Post-formation secondary mechanisms, including re-equilibration, microbial  
443 methane oxidation, and diffusive transport, have been proposed to explain the  
444 variations in clumped isotope composition that do not align well with the  
445 thermodynamic equilibrium (Beaudry et al., 2021; Giunta et al., 2021; Giunta et al.,  
446 2022; Jautzy et al., 2021; Krause et al., 2022; Labidi et al., 2020; Liu et al., 2023; Ono  
447 et al., 2021; Shuai et al., 2018; Stolper et al., 2015; Young et al., 2017).  
448 Re-equilibration is referred to the process that alters the original clumped isotopic  
449 compositions toward or along the thermodynamic equilibrium at a temperature range  
450 or condition either comparable with or drastically different from the current in situ  
451 setting. Because the re-equilibration takes place with intra-molecular re-ordering, the  
452 bulk isotopic compositions could have remained unaltered (Giunta et al., 2021; Labidi  
453 et al., 2020). The mechanism has been used to account for the origins of methane from  
454 the Precambrian continental shield, hydrothermal systems, Baltic Sea sediments, and

455 seep sediments from the Marmara Sea (Ash et al., 2019; Giunta et al., 2021; Labidi et  
456 al., 2020). The interpretation becomes even more appealing when the bulk isotopic  
457 compositions are apparently kinetic controlled (e.g., microbial methanogenesis) and  
458 clumped isotopic compositions reflects a state of or close to the thermodynamic  
459 equilibrium (Ash et al., 2019; Giunta et al., 2022; Ono et al., 2021).

460 To assess this inference, the probability of data distribution for  $\Delta^{13}\text{CH}_3\text{D}$  and  
461  $\Delta^{12}\text{CH}_2\text{D}_2$  values for mud volcanoes in western Taiwan and offshore sediments were  
462 plotted considering their structural configuration and hosted formations might  
463 resemble each other (Figure S4). Like that reported by Giunta et al. (2021), the  
464  $\Delta^{13}\text{CH}_3\text{D}$  values were scattered across the measured range and did not exhibit any  
465 pattern that demonstrated the clustering within a particular interval. In contrast, the  
466  $\Delta^{12}\text{CH}_2\text{D}_2$  values clustered within two broad ranges (0-8‰ and 12-17‰) if a 1‰  
467 interval was chosen. The bi-modal data distribution became even more prominent if a  
468 2‰ interval was used (Figure S4). The re-equilibration hypothesis lies on the premise  
469 that the intra-molecular re-ordering of  $^{12}\text{CH}_2\text{D}_2$  proceeds at a rate much faster  
470 (probably 2 times higher) than  $^{13}\text{CH}_3\text{D}$ . Therefore, over the course of re-equilibration,  
471  $\Delta^{13}\text{CH}_3\text{D}$  values produced by kinetic reactions (e.g., methanogenesis or thermal  
472 maturation) would vary toward the equilibrium line while  $\Delta^{12}\text{CH}_2\text{D}_2$  values remain at  
473 a relatively invariant range. Under this circumstance, the estimated temperature  
474 projected by clustering  $\Delta^{12}\text{CH}_2\text{D}_2$  values could be used to infer the possible  
475 temperature of re-equilibration, whereas  $\Delta^{13}\text{CH}_3\text{D}$  values represent the degrees of  
476 partial re-equilibration. The inference of re-equilibration described above is not  
477 favored based on the following arguments.

478 (1) The two clusters of  $\Delta^{12}\text{CH}_2\text{D}_2$  values obtained in this study could be  
479 translated into the estimated temperatures of  $60\pm 10^\circ\text{C}$  and  $200\pm 50^\circ\text{C}$  (Figure S4b).  
480 The lower one ( $60\pm 10^\circ\text{C}$ ) is derived from the samples collected from the Chishan  
481 fault (SYNH-01 and WSD) and offshore sediments. All samples from the Chishan  
482 fault possess bulk isotopic compositions interpreted as thermogenic methane, and  
483  $\Delta^{13}\text{CH}_3\text{D}$  and  $\Delta^{12}\text{CH}_2\text{D}_2$  values close to the equilibrium curve. For comparison, bulk  
484 isotopic compositions of methane for marine sediments indicate typical microbial  
485 origin. If the hypothetical re-equilibration proceeds with the variation in  $\Delta^{13}\text{CH}_3\text{D}$   
486 value only, the re-equilibration would occur at the temperature ( $60\pm 10^\circ\text{C}$ ), which is  
487 lower than the gas window commonly considered for the formation of thermogenic

488 methane ( $>80^{\circ}\text{C}$ ) (Pepper & Corvi, 1995). The scenario is unlikely unless the catalyst  
489 involved in the re-equilibration is sufficiently efficient to facilitate the intra-molecular  
490 re-ordering of methane isotopologues at that low temperature. Instead, the data  
491 distribution (both bulk isotopic and clumped compositions) could be best explained  
492 by the mixing between a thermogenic end component and a microbial end component  
493 represented by the offshore sediments (Figure S5; see section 5.3 for details).

494 (2) The cluster with higher projected temperatures ( $200\pm 50^{\circ}\text{C}$ ) (Figure S4b)  
495 encompasses several sub-clusters spanning over 30‰ of  $\Delta^{12}\text{CH}_2\text{D}_2$  values. Values off  
496 the equilibrium line were derived from samples collected from the Chukou fault,  
497 Chishan fault, Gutingkeng anticline, and Coastal Plain. For samples from the Chukou  
498 and Chishan faults, the majority of their  $\delta^{13}\text{C}$  and  $\delta^2\text{H}$  values are interpreted as  
499 thermogenic in origin (with the exception of YSES). For comparison, all samples  
500 from the Gutingkeng anticline and Coastal Plain possessed  $\delta^{13}\text{C}$  and  $\delta^2\text{H}$  values  
501 categorized as a mixture of microbial and thermogenic origin. By examining the  
502 details, the projected temperatures of re-equilibration based on  $\Delta^{12}\text{CH}_2\text{D}_2$  values  
503 range around  $200^{\circ}\text{C}$  and could reach as high as  $686^{\circ}\text{C}$  (Table S2). If the former  
504 projected temperature represents a temperature of re-equilibration, the  
505 re-equilibration would proceed with a burial of approximately 7 km depth (assuming  
506 the geothermal gradient is  $25^{\circ}\text{C}/\text{km}$ ; Chi and Reed, 2008) following the initial  
507 formation through either microbial process or thermal maturation. Since the  
508 disequilibrium clumped isotopic composition for thermogenic methane has not been  
509 affirmatively validated for environmental samples (Shuai et al., 2018; Xia & Gao,  
510 2019), only the scenario for the re-equilibration of microbial methane is addressed  
511 here. Although the temperature limit to life or methanogenesis could range up to  
512  $122^{\circ}\text{C}$  (Takai et al., 2008), the formation of microbial methane in petroleum or natural  
513 gas systems is generally considered to take place at temperature less than  $80^{\circ}\text{C}$  (Head  
514 et al., 2003). In this regard, at least additional  $\sim 5$  km of burial after its initial formation  
515 is presumably needed to reach the temperature for the designated re-equilibration. To  
516 assess this possibility, the uplift history of Taiwan orogenesis that has accommodated  
517 the shortening between the Luzon arc and the Eurasian plate is utilized. While the  
518 collision started at about 5 Ma (based on the first appearance of slate fragments in the  
519 sedimentary records; Teng, 1987), the uplift and exhumation accelerated during the  
520 period of 1-2 Ma (Chen et al., 2023; Lee et al., 2022). If the uplift rate of 1 cm/yr is

521 assumed (Chen et al., 2023; Yen et al., 2008), a total of 1000-2000 m of uplift would  
522 be expected. The estimate does not take erosion (up to 5 mm/yr based on  $^{10}\text{Be}$  dating;  
523 Fellin et al., 2017) into account and should be considered an optimum scenario. This  
524 quantity could also be translated into the burial of the formations in the footwall of  
525 thrust faults. Unless the uplift rate could be raised by at least a factor of 2.5 and the  
526 erosion could be ignored, the estimated optimum burial is apparently not sufficient to  
527 reach the designated re-equilibration temperature.

528 (3) Some of the data points for the high temperature cluster were distributed at  
529  $\Delta^{12}\text{CH}_2\text{D}_2$  values of less than 4 (samples collected from the Chukou fault, Gutingkeng  
530 anticline, and Coastal Plain). If these data points are attributed to the hypothetical  
531 re-equilibration, then the re-equilibration temperatures could be at least 261°C and  
532 reach as high as 686°C (Table S2). Such a temperature range requires an unlikely  
533 burial depth as being described and exceeds the upper bound for thermal maturation.  
534 Again, the data distribution could not be accounted for by re-equilibration.

535 For microbial methane oxidation, bulk isotope compositions for residue methane  
536 would generally increase with the extent of consumption (Whiticar, 1999). Depending  
537 on the fractionation factors, the enrichment in heavier isotopes would vary  
538 considerably among species or environmental characteristics. In contrast, the  
539 clumped isotopic compositions exhibit drastically different patterns between aerobic  
540 and anaerobic methane oxidation based on culture, enrichment, and environmental  
541 observations. The  $\Delta^{13}\text{CH}_3\text{D}$  and  $\Delta^{12}\text{CH}_2\text{D}_2$  values either decrease off or along the  
542 equilibrium curve for aerobic methane oxidation (Giunta et al., 2022; Krause et al.,  
543 2022), or cluster close to or along the equilibrium curve and its extension off 0°C  
544 mark or vary off the equilibrium curve and along the  $\Delta^{12}\text{CH}_2\text{D}_2$  axis for AOM (Ash et  
545 al., 2019; Giunta et al., 2022; Liu et al., 2023; Ono et al., 2021). In one case for the  
546 Baltic Sea sediments (Ash et al., 2019), a methanogenic zone is sandwiched by two  
547 sulfate-methane transition zones (SMTZ) attributed to the sulfate- and Fe-AOM. The  
548  $\Delta^{13}\text{CH}_3\text{D}$  and  $\Delta^{12}\text{CH}_2\text{D}_2$  values for the deep SMTZ are nearly constant, reaching a  
549 thermodynamic equilibrium at a temperature consistent with the in situ 7.8°C. The  
550 results obtained from the Black Sea sediments, on the other hand, exhibit a different  
551 pattern (Giunta et al., 2022). Their  $\Delta^{13}\text{CH}_3\text{D}$  and  $\Delta^{12}\text{CH}_2\text{D}_2$  values are close to the  
552 equilibrium curve at the bottom of SMTZ and increase to a highly enriched level  
553 (15-16‰ for  $\Delta^{13}\text{CH}_3\text{D}$  and 60-75‰ for  $\Delta^{12}\text{CH}_2\text{D}_2$ ) at the top of the SMTZ, a pattern

554 also observed in the incubations of AOM enrichments from Svalbard sediments (Liu  
555 et al., 2023). For comparison, the potential AOM in seep sediments (from Santa  
556 Barbara Channel) and deep materials (Nankai sediments and Beatrix fluids) shift the  
557  $\Delta^{13}\text{CH}_3\text{D}$  value toward the thermodynamic equilibrium with the insignificant change  
558 in  $\Delta^{12}\text{CH}_2\text{D}_2$  value (Liu et al., 2023). The contrast patterns of isotopologue  
559 abundances have been linked to the reversibility of methane oxidation potentially  
560 controlled by the thermodynamic drive intrinsically linked to the availability of  
561 sulfate and methane (Liu et al., 2023). For abundant substrate (and energy flow) like  
562 that attested by culture experiments (Ono et al., 2022), AOM is regulated by kinetic  
563 effects that lead to the disequilibrium isotopologue abundances. In contrast, AOM  
564 imposed by limited substrate availability proceeds with the high reversibility so  
565 thermodynamic equilibrium could be readily reached (Liu et al., 2023). Various  
566 thresholds of the substrate availability have been proposed primarily based on field  
567 observations (Ash et al., 2019; Giunta et al., 2022; Ono et al., 2021), thereby  
568 warranting the validation from laboratory tests.

569 To address the potential of AOM for this study, the distribution of  $\Delta^{13}\text{CH}_3\text{D}$  and  
570  $\Delta^{12}\text{CH}_2\text{D}_2$  values was first examined. Only two seep sediments (FWCR and FR)  
571 possess  $\Delta^{13}\text{CH}_3\text{D}$  and  $\Delta^{12}\text{CH}_2\text{D}_2$  values resembling those from the Baltic and Black  
572 Seas near the equilibrium curve at the low temperature end. However, these two  
573 sediments were retrieved from the gas hydrate stability zone at a depth of 108 m for  
574 FWCR and 22 m for FR below the seafloor. Based on the geochemical characteristics  
575 (Bohrmann et al., 2023), these samples are not representative of sediments typical for  
576 AOM. Furthermore, the data points for mud volcanoes in western Taiwan (Figure S4)  
577 are not near the low temperature end of the equilibrium line but resemble the shift  
578 caused by potential AOM that proceeds with high reversibility under or near  
579 thermodynamic threshold (Liu et al., 2023). Although sulfate-AOM at <10 cm depth  
580 has been validated based on the geochemical profile and genetic data for SYNH  
581 (Cheng et al., 2012; Lin et al., 2018), these samples were collected from the mud  
582 platform formed by the accumulation of fluidic mud emanating from the bubbling  
583 pool. Here, sulfate-AOM is fueled by methane percolating off the major fluid conduit  
584 and through the porous medium, and by sulfate generated by the oxidation of pyrite or  
585 iron sulfide through the exposure of deeply sourced sediments to the atmosphere  
586 (Cheng et al., 2012; Lin et al., 2018). As our samples were collected from the

587 bubbling pools that represent the surface expression of subsurface fluid channels,  
588 collected gases were plumbed from the deep source with minimum alteration during  
589 the transport, thereby exhibiting geochemical and community composition patterns  
590 distinct from those in the mud platform (Cheng et al., 2012; Lin et al., 2018). Similarly,  
591 aerobic methane oxidation has been validated with geochemical, incubation, and  
592 genetic data for the mud platform sediments at SYNH (Cheng et al., 2012; Lin et al.,  
593 2018). Again, companion data for samples collected from bubbling pools are distinct  
594 from those from the mud platform. The bulk and clumped isotopic compositions for  
595 our samples were also not aligned with the ranges commonly attributed to aerobic  
596 methane oxidation (Figures 2 and 3). Taken together, while these lines of evidence do  
597 not favor microbial methane oxidation (either anaerobic or aerobic style) as the main  
598 cause of isotopic variations, the possibility of AOM could not be completely ruled  
599 out.

600 Finally, molecular diffusion has been considered to address the isotopic  
601 variations (both bulk and clump isotopes) (Giunta et al., 2021). The tenuous nature of  
602 diffusive pathway in sedimentary rocks would particularly enable the  
603 mass-differentiation transport during fluid percolation over a long-distance range.  
604 According to the rules of mass difference (Etiopie et al., 2009), diffusion facilitates to  
605 transport lighter isotopes over heavier ones, resulting in the preferential depletion of  
606  $^{13}\text{C}$  or smaller  $\delta^{13}\text{C}/\delta^2\text{H}$  values for migratory methane (or vice versa for residue  
607 methane). On the other hand, the corresponding  $\Delta^{12}\text{CH}_2\text{D}_2$  vs.  $\Delta^{13}\text{CH}_3\text{D}$  values would  
608 increase (Giunta et al., 2021). Both these variation trends follow a 1:1 slope in the  $\delta^2\text{H}$   
609 vs.  $\delta^{13}\text{C}$  and  $\Delta^{12}\text{CH}_2\text{D}_2$  vs.  $\Delta^{13}\text{CH}_3\text{D}$  plots (Figure S4; constrained by the beta value  
610 (0.05) for single or double substituted isotopologues). Either plot for the data reported  
611 in this study reveals that diffusion seems to account for multiple linear distributions of  
612 isotopic compositions (Figure S4). However, if a  $\delta^{13}\text{C}$  value of -33‰ (CLP;  
613 thermogenic methane) is used to anchor one end of the diffusion trend in the plot of  
614  $\Delta^{13}\text{CH}_3\text{D}$  vs.  $\delta^{13}\text{C}$  (Figure S4), it is apparent that the variations in  $\delta^{13}\text{C}$  value is not  
615 sufficient to account for those in  $\Delta^{13}\text{CH}_3\text{D}$  value (nearly all data points plotted above  
616 the diffusion trend). If diffusion is the governing mechanism for isotopic fractionation,  
617 the anchor point in  $\delta^{13}\text{C}$  axis has to be set at a higher value ( $> -20\text{‰}$ ), a scenario more  
618 likely representing abiotic source and not supported by the current data. Again,  
619 diffusion could not explain the data variation.

620 Overall, the data pattern, geological context, and the projected temperature based  
621 on individual isotopologue abundance are not in favor of the re-equilibration,  
622 microbial methane oxidation, and diffusive transport as a broad-scaled control on the  
623 variations in bulk and clumped isotopic compositions. For those clumped isotopic  
624 compositions off the equilibrium line, the mixing between thermogenic and microbial  
625 sources appears to be the most plausible explanation for most samples (see section 5.3  
626 for details). Since these samples are distributed in several structural domains, the  
627 exchange of fluids and gases between domains is unlikely. Lumping all data together  
628 across structural domains could have potentially masked the intrinsic characteristics  
629 associated with primary and secondary mechanisms responsible for the formation or  
630 alteration of methane for individual structural domains or samples. To unequivocally  
631 discern methane origins in such a tectonically complex and fragmented terrain like  
632 Taiwan, a wider coverage of sampling with designated targets and designed  
633 laboratory experiments is warranted.

634

### 635 5.3 Mixing of methane, helium, and nitrogen between sources

636 The isotopologue abundances provide an extra dimension to account for a  
637 mixed origin, in addition to bulk isotopic compositions and abundance ratios. The  
638 mixing scenarios are discussed here in accordance with the structural domains. As the  
639 exact mechanisms and characteristics of abiotic methane are still vague, the mixing  
640 scenarios are limited to using thermogenic and microbial end components. In  
641 principle, the highest estimated temperatures based on isotopologue abundances for  
642 the individual structural domain were selected as the thermogenic end component.  
643 Results obtained from culture experiments (Young et al., 2017; Giunta et al., 2019)  
644 were first used as the microbial end component. Other than that, environmental  
645 samples indisputably attributed to methanogenesis could also be considered. To avoid  
646 of arbitrary designation, it would be even better if the target samples and  
647 environmental samples treated as the end component could belong to a similar/same  
648 geological context. Therefore, the potential heterogeneity of the end component  
649 compositions would be taken into account. Regardless of which end component is  
650 chosen, the mixing scenarios based on bulk and clumped isotopic compositions  
651 should be coherent. For sites along the Chishan fault, methane from some sites  
652 (SYNH-01 and WSD-01) was partially produced by secondary CO<sub>2</sub> reduction (see

653 section 5.1). Their bulk isotopic compositions slightly deviated from the potential end  
654 component of thermal maturation ascribed to SYNH-02. To quantify the contribution  
655 of thermogenic versus microbial methane, mass conservation was first applied with a  
656 thermogenic end component represented by  $\delta^{13}\text{C}_{\text{CH}_4}$  of -35.3‰ and  $\delta^2\text{H}_{\text{CH}_4}$  of  
657 -143.6‰ (site SYNH-02), and a microbial end component represented by average  
658 culture values for either  $\text{CO}_2$  reduction methanogenesis ( $\delta^{13}\text{C}_{\text{CH}_4}$  of -51.1‰ and  
659  $\delta^2\text{H}_{\text{CH}_4}$  of -389.4‰) or methylotrophic methanogenesis ( $\delta^{13}\text{C}_{\text{CH}_4}$  of -45.8‰ and  
660  $\delta^2\text{H}_{\text{CH}_4}$  of -299.4‰) (Young et al., 2017; Giunta et al., 2019). For sites SYNH-01 and  
661 WSD-01, their similar bulk isotopic compositions both yielded 10% and 25%  
662 contributions of microbial methane from  $\text{CO}_2$  and methylated compounds,  
663 respectively (Figure S5). Similar approaches were adopted in the isotopologue mixing  
664 model ( $\Delta^{13}\text{CH}_3\text{D}$  of 2.13‰ and  $\Delta^{12}\text{CH}_2\text{D}_2$  of 5.47‰ from site SYNH-02 for the  
665 thermogenic end component;  $\Delta^{13}\text{CH}_3\text{D}$  of 2.90‰ and  $\Delta^{12}\text{CH}_2\text{D}_2$  of -16.46‰ from  
666 methanogens in laboratory (Giunta et al., 2019; Young et al., 2017) as the average  
667 microbial end component). The calculation yielded a 60% microbial fraction for site  
668 SYNH-01, and 45% for site WSD-01, from  $\text{CO}_2$  reduction methanogenesis (Figure  
669 S5). For comparison, the isotopologue mixing model based on methylotrophic  
670 methanogenesis could not replicate the observations.

671 Marine sediments collected offshore Taiwan (FR and FWCR) as the potential  
672 microbial end component were also assessed. These two samples possessed bulk  
673 isotopic compositions typical for microbial methane ( $\delta^{13}\text{C}_{\text{CH}_4}$  of -69‰ and  $\delta^2\text{H}_{\text{CH}_4}$  of  
674 -190‰). Their clumped isotopic compositions were, however, distinct from the  
675 culture representatives, and distributed off the equilibrium line (Figure 2) in the space  
676 occupied with a number of data points from marine sediments (Ash et al., 2019;  
677 Giunta et al., 2022). The mixing scenarios are not coherent between clumped and bulk  
678 isotopic compositions. While the isotopologue mixing model yielded a microbial  
679 contribution ranging from 20% to 60% (Figure S5), the bulk-based mixing model  
680 yielded a much less microbial contribution (<10%) with greater uncertainties.

681 For sites in the Chukou fault, the Gutingkeng anticline, and the Coastal Range, a  
682 mixing model was constructed using a similar thermogenic end component (KTL for  
683 the Chukou fault, SYNH-02 for the Gutingkeng anticline, and LS for the Coastal  
684 Range) and a microbial end component derived from marine sediments (either  
685 FR/FWCR values or  $\delta^2\text{H}_{\text{CH}_4}$  and  $\Delta^{12}\text{CH}_2\text{D}_2$  values slightly smaller than FR/FWCR

686 values). The calculations for bulk isotopic and isotopologue mixing yielded  
687 comparable fractions (40% to 80% for bulk isotope mixing and 20% to 90% for  
688 isotopologue mixing) of the microbial end component (Figure S5), a pattern  
689 consistent with the detection of methanogens using different substrates in these  
690 regions (Chang et al., 2012; Ling et al., 2012; Wang et al. 2014).

691 Helium isotopic ratios ranged from 0.1 to 6.8 Ra (Figure 3; Table S4). Most ratios  
692 (except for sites AT, CLP, CLS, TDS, GI, and LS) were smaller than 1 Ra, indicating  
693 that the gases originated from a crustal component. The N<sub>2</sub> isotopologue results  
694 appear to be correlated with helium isotopes. Three sites (KTL-02, WSD-01, and AT)  
695 showed  $\Delta_{30}$  values ranging between +11‰ and +17‰ (Figure S3; Table S3;). This is  
696 lower than the air value of +19.3‰ (Yeung et al., 2017) but much higher than 0‰  
697 observed for crustal and volcanic nitrogen (Labidi et al., 2020), suggesting the  
698 addition of the air to deep crustal/volcanic nitrogen. A mass balance calculation  
699 yielded that 40-80% of the N<sub>2</sub> in the gas mixtures must be accounted for by the  
700 air-derived nitrogen. In other words, the nitrogen with a deep origin with a  $\Delta_{30}$  value  
701 of 0‰ (Labidi et al., 2020) contributed to 20-60% of the gas mixtures. While no  
702 robust  $\delta^{15}\text{N}$  estimate could be provided for the crustal nitrogen end component,  $\delta^{15}\text{N}$   
703 values tend to vary towards a more negative range (-2.1‰) for the samples with the  
704 highest air contributions. This likely reflects mass-dependent fractionation of  
705 atmospheric nitrogen in the subsurface (Labidi and Young, 2022), rather than a  
706 signature from deep nitrogen. The  $\Delta_{30}$  pattern for KTL and WSD in the Western  
707 Foothills is consistent with crustal helium signatures and methane formations at  
708 temperatures of 260°C (for KTL). However, the deep nitrogen source for AT in the  
709 Coastal Range is not necessarily only the crustal component. Its  $^3\text{He}/^4\text{He}$  ratio is  
710 relatively high (2.3 Ra), suggesting a mixture between mantle and air/crust. The bulk  
711 and clumped isotopic compositions of methane are interpreted as the abiotic origin  
712 with the formation temperature or depth unconstrained (see sections 5.1 and 5.4 for  
713 details). If nitrogen shares the same source of helium, the deep source is at least  
714 partially composed of the mantle component. For comparison, the two GI duplicates  
715 with 6.7 Ra and 6.8 Ra showed  $\Delta_{30}$  values of 3.1‰ and 1.8‰, a range close to 0‰.  
716 This likely reflects marginal (<10%) air contributions. Their  $\delta^{15}\text{N}$  values were +3.6‰,  
717 a pattern consistent with the signature associated with subducted nitrogen, which is  
718 later accumulated in sub-arc mantle sources worldwide (Busigny et al., 2011, Epstein

719 et al., 2021, Labidi et al., 2021), and previously hypothesized to contribute nitrogen to  
720 surface vents in Taiwan (Rouilleau et al., 2015). Together with mantle-derived helium,  
721 the recycled nitrogen must have been remobilized towards the surface via volcanism  
722 followed by hydrothermal interactions.

723 While the origins of methane from sites CLP, CLS, TDS, and LS could be  
724 constrained by bulk isotopic and isotopologue compositions, and abundance ratios  
725 (thermogenic for sites CLP, CLS and LS, and microbial for site TDS), their  
726 anomalous helium isotopic compositions deserve special attentions. The analyses  
727 yielded  $^3\text{He}/^4\text{He}$  ratios that ranged from 1.8 Ra (TDS and LS) to 5.4 Ra (CLP and CLS)  
728 and were comparable with data reported previously for sites CLP, CLS (Fu et al.,  
729 2021), and LS (Yang et al., 2003). The values suggest a mixture between crustal (0.01  
730 Ra) and mantle components (>8 Ra) (Poreda & Craig, 1989). Except for site LS, the  
731 involvement of a mantle contribution is intriguing since the other three sites are all  
732 part of the accretionary prism with sporadic volcanism that dates back to 17 Ma and is  
733 potentially associated with the opening of the South China Sea (Chen, 2016). These  
734 igneous rocks in the subsurface might serve to account for the continuous degassing  
735 of helium with mantle signatures. Alternatively, the supply of helium with mantle  
736 signatures could have been along the fault or fracture network extending to the mantle  
737 depth. In this regard, helium with mantle signatures should have pervasively  
738 infiltrated into the fracture systems of the accretionary prism and been observed at a  
739 regional scale, which is not the case in this study. For site LS, the impingement of the  
740 Luzon Arc on the Eurasian continent has emplaced numerous igneous bodies in the  
741 Coastal Range. Like what has been observed for site GI, helium with mantle  
742 signatures could have originated from the igneous intrusion in the subsurface.  
743 Regardless of the source region, methane and hydrocarbons from igneous bodies are  
744 generally considered to possess abiotic signatures, which were not observed for sites  
745 associated with sedimentary formations (CLP, CLS, TDS, and LS) but were  
746 consistent with the arc setting for sites AT and GI.

747 Overall, the origins of methane, helium, and nitrogen gases could have been  
748 segregated into different compartments of the subduction system. Therefore, their  
749 individual mixing patterns would not be necessarily coupled but rather reflect the  
750 complexity of sources, transport paths, and fracture connectivity in the tectonically  
751 fragmented terrain of Taiwan.

752

#### 753 5.4 Potential abiogenic methane in the Coastal Range

754 The methane recovered from sites AT and GI is interpreted as originating from  
755 abiotic Fischer-Tropsch Type processes. Their  $\Delta^{13}\text{CH}_3\text{D}$  and  $\Delta^{12}\text{CH}_2\text{D}_2$  values  
756 (Figure 2) overlap with the range for abiotic methane reported in previous studies  
757 (Young et al., 2017) and are distributed near (for site GI) or on the equilibrium line  
758 (for site AT; corresponding to  $\sim 23^\circ\text{C}$ ) (Figure 2). Laboratory constraints have shown  
759 that such surface catalyzed reactions between hydrogen and CO or  $\text{CO}_2$  on different  
760 metal sulfides proceed at temperatures between  $70^\circ\text{C}$  and  $600^\circ\text{C}$  (Etiope & Lollar,  
761 2013). Field observations and interpretations that combined bulk isotopic  
762 compositions, abundance ratios, and water/geological characteristics for regions with  
763 prevalent serpentinization have further extended the possible temperature to between  
764  $50^\circ\text{C}$  and  $500^\circ\text{C}$  (Etiope & Lollar, 2013). Limited experiments, however, have shown  
765 that methane synthesized from the Sabatier reactions catalyzed by Ru at  $70\text{-}600^\circ\text{C}$   
766 yielded  $\Delta^{13}\text{CH}_3\text{D}$  and  $\Delta^{12}\text{CH}_2\text{D}_2$  values either on the high temperature end of the  
767 equilibrium line ( $>400^\circ\text{C}$ ) or distributed over a wide range below the equilibrium line  
768 ( $\Delta^{13}\text{CH}_3\text{D}$  between  $0\text{‰}$  and  $+4.5\text{‰}$  and  $\Delta^{12}\text{CH}_2\text{D}_2$  between  $-55\text{‰}$  and  $0\text{‰}$ ) (Young et  
769 al., 2017). For comparison,  $\Delta^{13}\text{CH}_3\text{D}$  and  $\Delta^{12}\text{CH}_2\text{D}_2$  values for Chimaera and Kidd  
770 Creek samples attributed to abiogenic in origin are distributed either along the segment  
771 of the equilibrium line between  $25^\circ\text{C}$  and  $150^\circ\text{C}$  or below the equilibrium line (Young  
772 et al., 2017). The data pattern obtained in this study is distinct from the experimental  
773 constraints but resembles the field observations. However, the temperature estimate  
774 based on isotopologue abundances is much lower than the field observation for site  
775 AT ( $23^\circ\text{C}$  versus  $62^\circ\text{C}$ ). Such temperature contradiction suggests that both  
776 isotopologues do not reach internal equilibrium and thus do not record a true  
777 formation temperature. In addition, helium isotopic compositions for sites GI and AT  
778 were 6.7 Ra and 2.4 Ra, respectively (Table S4). This range of helium isotope  
779 compositions suggests a higher mantle fraction and is comparable with the proximity  
780 to igneous bodies associated with the arc impingement. Overall, the close  
781 resemblance of isotopologue abundances between these two sites and Chimaera/Kidd  
782 Creek combined with the higher contribution of mantle helium reinforces the  
783 interpretation that methane from these two sites is abiogenic in origin. The formation  
784 could have proceeded at temperatures slightly lower than those imposed by

785 experimental constraints. Alternatively, post-formation resetting of abiogenic methane  
786 isotopologues, dominated by changes in  $\Delta^{12}\text{CH}_2\text{D}_2$  as described by Labidi et al. (2020)  
787 might explain the shift from a purely abiogenic isotopologue signature to one near  
788 equilibrium at lower temperatures, although the temperature disparity remains. The  
789 possibility that the abiogenic-like signatures are derived from AOM (Warr et al., 2021;  
790 Giunta et al., 2022; see section 5.2 for more discussion), thermal maturation of  
791 organic matters circulated from surface waters (Fiebig et al., 2019) or biodegradation  
792 of organic matters with  $\text{H}_2$  produced by serpentinization (Xia & Gao, 2021) is noted.

793

#### 794 5.5 Water isotopic compositions

795 Isotopic compositions of water fell within the range reported previously (Chao  
796 et al., 2011; You et al., 2004). Among data points, several for sites LS and AT in the  
797 Coastal Range, and site WF in the Chukou fault were distributed near or along the  
798 global and local meteoric water lines (Peng et al., 2010; Figure 4a). While data  
799 points for site GI clustered around a seawater composition (Table S5), all the other  
800 data points deviated from the meteoric water line and exhibited various degrees of  
801  $^{18}\text{O}$  enrichment (Figure 4a). By combining with previous results, two variation  
802 trends could be drawn. The first one is composed of data points for the Chishan fault,  
803 Gutingkeng anticline, and Coastal Plain, whereas the second one comprises data  
804 points solely from the Chukou fault. Both trends share a common end component  
805 enriched with  $^{18}\text{O}$  ( $\delta^{18}\text{O}_{\text{H}_2\text{O}}$  values were +7‰). The presence of such an  $^{18}\text{O}$ -enriched  
806 water is also observed in a previous study for the porewater retrieved from the TY  
807 mud volcano offshore southwestern Taiwan, and could best be accounted for by deep  
808 water derived from the smectite dehydration at 100-150°C (Chen et al., 2020). Using  
809 the average geothermal gradient for the offshore region (25°C/km; Chi and Reed,  
810 2008), the depth corresponding to the water formation has been estimated to range  
811 between 3.6 km and 5.7 km below the seafloor (Chen et al., 2020). If this end  
812 component is prevalent in the accretionary wedge across marine and terrestrial realms,  
813 the water mixture would be bracketed by three end components, including deep  
814 water (stated above), seawater-like water, and meteoric water.

815 For sites in the Chishan fault, Gutingkeng anticline, and Coastal Plain, the data  
816 distribution (Figure 4a) suggests a greater contribution of seawater-like water over  
817 meteoric water. Except for site TDS, most mud volcanoes in western Taiwan are

818 located at least 10 km from the shoreline (Figure S1). Therefore, the scenario of the  
819 seawater intrusion is less likely. Instead, the seawater-like composition could have  
820 been derived from relic seawater trapped during sedimentation. In contrast, for sites  
821 in the Chukou fault, the data distribution is aligned clearly with an end component  
822 comparable with the compositions of meteoric water retrieved from the southern  
823 plain or mountains (Peng et al., 2010).

824 Finally, the involvement of an end component resembling meteoric water  
825 suggests a short residence time of water circulation. Constraining the exact age or  
826 residence time of water from mud volcanoes is challenging as the tracers available for  
827 such a geological context are limited, and no data has been published to date. Site LS  
828 was chosen as an example to constrain the potential limit for the circulation of  
829 meteoric water as its water isotopic compositions fell on the local meteoric water line.  
830 Based on the isotopologue abundances, the temperature and depth for methane  
831 formation for site LS were estimated to be up to 90-100°C and 2-3 km below the land  
832 surface, respectively. If this depth limit to the circulation of meteoric water is also  
833 applied to all mud volcanoes in the Western Foothills, a fast-track path from recharge  
834 of meteoric water to discharge along the fracture network at depths of less than 3 km  
835 would be required. To accommodate this possibility, the fracture opening derived  
836 from the depressurization and thrust displacement related to the rapid uplift and  
837 erosion is speculated to enable bedrock more permeable for recharge and deep  
838 penetration of water. The inference might not be the unique cause for tectonically  
839 fragmented terrains with rapid uplift and erosion (Chen et al., 2015; Dadson et al.,  
840 2003), as previous studies have demonstrated that isotopic compositions of cored  
841 calcite veins from a 2000-m deep borehole (Wang et al., 2010) and hot springs  
842 sampled from northern Taiwan are indicative of meteoric in origin (Chao et al., 2021;  
843 Lu et al., 2020). These results suggest that meteoric water could be recharged and  
844 circulated to deeper regions, heated up by the exhumed bedrocks that still preserve the  
845 relic heat associated with rapid uplift, and discharged along the fracture network to the  
846 surface outcrops.

847 The isotopic compositions of water suggest water circulation along different  
848 paths and the contribution of water compartmentalized in different source regions.  
849 For most samples from eastern Taiwan and few from western Taiwan, the meteoric  
850 nature further implied that water circulation is rapid with a short residence time in

851 the subsurface. Therefore, isotopic exchange between water and minerals is not  
852 substantially enough to alter the resultant water composition. In contrast, the  
853 majority of samples from western Taiwan bear the contribution of deep water that  
854 has experienced prolonged water-rock/mineral interactions. Water circulation along  
855 the divergent, and complex fracture network in the accretionary wedge enables the  
856 mixing process of deep water with either the formation water or meteoric water at  
857 shallow depths.

858 In addition to water origins, water isotopic compositions were used to constrain  
859 source characteristics of both water and methane. Estimated temperatures based on  
860 deuterium exchange between water and methane were compared with temperatures  
861 assessed by methane isotopologue abundances. The thermometer is adopted from  
862 Horibe and Craig (1995) using the following equation (for temperatures between 0°C  
863 and 370°C):

864

$$865 \alpha(\text{H}_2\text{O}_{\text{Liq}}/\text{CH}_4) = 1.0997 + 8456/T^2 + 0.9611 \times 10^9/T^4 - 27.82 \times 10^{12}/T^6 \quad \text{eq. 8}$$

866

867 where  $\alpha$  is the ratio of  $^2\text{H}/^1\text{H}$  of water to methane, and T is in Kelvin.

868 For sites CLP, CLS, SYNH-02, and WD where isotopologue equilibrium is  
869 reached and deep water predominates over the other component, the temperatures  
870 estimated from the deuterium fractionations between methane and water ( $\epsilon_{\text{CH}_4\text{-H}_2\text{O}}$ )  
871 correspond closely to the temperatures predicted by  $\Delta^{13}\text{CH}_3\text{D}$  and  $\Delta^{12}\text{CH}_2\text{D}_2$  values  
872 (Figure 4; Table S5). Comparable temperature estimates could be obtained for two  
873 additional sites (sites SYNH-01, and LCW) if only  $\Delta^{13}\text{CH}_3\text{D}$  values were considered.  
874 For the equilibrium fractionation associated with deuterium exchange, two phases  
875 (methane and water) were involved. Therefore, comparable temperature estimates  
876 deduced from isotopic substitution within a phase and between phases suggest that  
877 methane and water shared a common source region, and the isotopic exchange  
878 between  $^{13}\text{CH}_3\text{D}$  and water is more rapid than between  $^{12}\text{CH}_2\text{D}_2$  and water. The  
879  $\Delta^{13}\text{CH}_3\text{D}/\Delta^{12}\text{CH}_2\text{D}_2$  values paired with  $\epsilon_{\text{CH}_4\text{-H}_2\text{O}}$  values for all the other sites fell off  
880 the equilibrium line (Figure 4). Since methane and water from these sites represent a  
881 mixture of different sources, isotopic exchange within a phase or between phases  
882 after mixing does not reach equilibrium, possibly due to insufficient time or a kinetic  
883 barrier imposed by the relatively low temperature. Finally, temperature estimates

884 based on paired isotopologue abundances were coherent for site LS in eastern  
885 Taiwan. However, the methane isotopologue abundances did not reach equilibrium  
886 with deuterium in the water. The data pattern contrasts with other studies (Giunta et  
887 al., 2019; Wang et al., 2015) and suggests that meteoric water percolating into the  
888 deep subsurface does not coexist with methane sufficiently long or methane is not  
889 completely dissolved in water to achieve isotopic equilibrium between phases. Again,  
890 consistent with the interpretation based solely on water isotopic compositions, the  
891 water circulation is likely rapid so the residence time is short.

892

### 893 5.6 Depth constraints using isotopologue-based temperature estimates

894 Our results indicated that the temperature estimates for sites CLP, CLS, KTL,  
895 SYNH-02, WD, and LS ranged from 99°C to 260°C (Table S2 and S6). Using  
896 measured local geothermal gradients (Chi & Reed, 2008) and assuming a surface  
897 temperature of 20°C, the methane generation depth was estimated to range from 2 to  
898 9 km. The sites where methane reaches internal equilibrium are primarily distributed  
899 in three major structural features: sites CLP, CLS, and KTL in the Chukou fault, site  
900 SYNH-02 in the Chishan fault, and site LS in the Longitudinal Valley fault. The  
901 Chukou fault is an east dipping thrust oriented NE-SW (Yeh et al., 2016). Balanced  
902 cross sections suggest that the fault probably represents a complex fault system with  
903 subsurface branches forming an imbricate structure and an anticline underneath (Yeh  
904 et al., 2016). The fault and its branches are generally parallel to bedding within the  
905 Miocene formation and could be considered as part of the detachment fault  
906 extending to a depth of 7-8 km. The depth estimate ranged from 7-8 km for site CLP,  
907 to 4-5 km for site CLS, and to 6-8 km for site KTL (Figure 5a). As the formations  
908 are deformed and fragmented, water and gas transport could follow multiple routes  
909 interconnected to each other. Therefore, the estimated depth could be representative  
910 of the detachment fault and its related fracture system. For comparison, the Chishan  
911 fault is a high-angled, east dipping thrust with a left lateral component, and  
912 represents one of the branches of the detachment fault propagating westward (Rau et  
913 al., 2012). The depth estimates for site SYNH-02 were 8–9 km (Figure 5b), a range  
914 deeper than that reported for sampling in 2017 (Rumble et al., 2018; Supporting  
915 information) and coinciding with the extension of the detachment fault (10-12 km)  
916 in the region (Chen, 2016). The occurrence is also consistent with the origin of

917 <sup>18</sup>O-enriched water retrieved from sites SYNH-01 and -02. Site WD is located  
918 further west of site SYNH-02 in the Coastal Plain and is not associated with any  
919 apparent fault outcrop. Based on seismic reflection, mud diapirism oriented NE-SW  
920 offshore this region has been identified (Chen et al., 2014). Site WD is aligned well  
921 with the onshore extension of one of the offshore mud diapirs. Whether the  
922 estimated formation depth of 7 km corresponds to the base of mud diapir or the  
923 detachment fault remains uncertain. Regardless of the source characteristics, its  
924 water isotopic composition is comparable with that of site SYNH-02 and the  
925 designated deep water. Finally, the Longitudinal Valley fault is the plate boundary  
926 thrust with a high angle dipping east and a left lateral sense (Chang et al., 2000). The  
927 hanging wall formation (Lichi formation) hosts site LS, and is composed of  
928 unlithified clays with rock fragments of various lithologies (e.g., ultramafic,  
929 meta-sandstone) (Chen et al., 2007). This combined with intensively shearing  
930 suggests its intimate relationship with the subduction. The depth estimate of 2-3 km  
931 (Figure 5c) for this site probably corresponds to a source region at the base of the  
932 Lichi formation intersected by the Longitudinal Valley fault.

933

## 934 6. Conclusions

935 Our methane isotopologue results combined with helium, nitrogen, water, and  
936 CO<sub>2</sub> related isotopic compositions reveal a spectrum of geochemical characteristics  
937 that point to diverse formation mechanisms and conditions for gases and water  
938 emanating from mud volcanoes, seeps, and springs investigated. Thermogenic  
939 methane was formed at temperatures ranging between 99°C and 260°C and appears to  
940 constitute a major component of hydrocarbons. The depths (2-9 km) corresponding to  
941 the estimated temperatures suggest a strong structural control that influences water  
942 and gas pathways. Thermogenic methane from a deep source is likely mixed by  
943 various degrees with abiotic methane pertinent to igneous bodies emplaced during  
944 subduction/collision, or microbial methane at shallow depths prior to being  
945 discharged to the atmosphere or seawater. Our results also suggest the potential  
946 decoupling of methane from water or helium sources, and an evolving depth range or  
947 mixing contribution for methane formation. Such patterns are consistent with active  
948 orogenesis, where gas and water channeling can undergo temporal and spatial  
949 variations associated with terrain fragmentation and dynamic structural control over

950 the course of mountain building.

951

### 952 *Acknowledgments*

953 We are grateful to the aid for sample and core retrievals by Nai-Chen Chen,  
954 Jui-Fen Tsai, Ling-Ho Chung, Tourism Bureau of Tainan City Government,  
955 Agriculture Bureau of Kaohsiung City Government, Zhaori Hot Spring of Taitung  
956 County Government, and the captain and crew members of R/V Sonne (cruise  
957 SO266/1). The MARUM-MeBo200 team and David Wunsch (CORSYDE  
958 International GmbH & Co. KG; Berlin) are sincerely thanked for the preparation and  
959 deployment of the MeBo pressure core samplers during cruise SO266/1. We extend  
960 our gratitude to Dr. George Burr at National Taiwan University for English editing  
961 this manuscript.

962 Grant supports from Taiwanese Ministry of Education and Ministry of Science  
963 and Technology (MOST107-3113-M-002-004) are acknowledged. Cruise SO266/1  
964 was funded by the German Ministry of Education and Science, project TaiDrill –  
965 SO266.

966

### 967 *Open Research*

968 All new data reported in the study are available on tables in the main manuscript  
969 and supporting information, and are archived at Lin et al. (2023).

970

### 971 *References*

- 972 Ash, J.L., Egger, M., Treude, T., et al. (2019). Exchange catalysis during anaerobic  
973 methanotrophy revealed by  $^{12}\text{CH}_2\text{D}_2$  and  $^{13}\text{CH}_3\text{D}$  in methane. *Geochemical*  
974 *Perspectives Letters*, 26-30. doi:10.7185/geochemlet.1910
- 975 Beaudry, P., Stefánsson, A., Fiebig, J., et al. (2021). High temperature generation and  
976 equilibration of methane in terrestrial geothermal systems: Evidence from clumped  
977 isotopologues. *Geochimica et Cosmochimica Acta*, 309, 209-234.  
978 doi:10.1016/j.gca.2021.06.034
- 979 Bernard, B.B., Brooks, J.M., & Sackett, W.M. (1977). A geochemical model for  
980 characterization of hydrocarbon gas sources in marine sediments. *Paper presented*  
981 *at the Offshore Technology Conference*. doi:10.4043/2934-MS
- 982 Bohrmann, G., Berndt, C., Lin, S., et al. (2023). Geological controls on the

983 distribution of gas hydrates in the shallow parts of the gas hydrate stability zone–  
984 constraints from seafloor drilling off Taiwan. *Marine and Petroleum Geology*,  
985 106253. doi:10.1016/j.marpetgeo.2023.106253

986 Bonilla, M.G. (1975). A Review of Recently Active Faults in Taiwan: U.S. Geological  
987 Survey Open-File Report 75-41 Version 1.1.

988 Busigny, V., Cartigny, P., & Philippot, P. (2011). Nitrogen isotopes in ophiolitic  
989 metagabbros: A re-evaluation of modern nitrogen fluxes in subduction zones and  
990 implication for the early Earth atmosphere. *Geochimica et Cosmochimica Acta*, 75,  
991 7502-7521. doi:10.1016/j.gca.2011.09.049

992 Campeau, A., Wallin, M. B., Giesler, R., et al. (2017). Multiple sources and sinks of  
993 dissolved inorganic carbon across Swedish streams, refocusing the lens of stable C  
994 isotopes. *Scientific reports*, 7, 9158. doi:10.1038/s41598-017-09049-9

995 Carson, B., & Sreaton, E.J. (1998). Fluid flow in accretionary prisms: Evidence for  
996 focused, time-variable discharge. *Reviews of Geophysics*, 36, 329-351.  
997 doi:10.1029/97rg03633

998 Central Geological Survey; <https://twgeoref.moeacgs.gov.tw>  
999 Central Weather Bureau;  
1000 <https://scweb.cwb.gov.tw/en-US/earthquake/details/2017021101125257008>

1001 Chang, C.P., Angelier, J., & Huang, C.Y. (2000). Origin and evolution of a mélange:  
1002 the active plate boundary and suture zone of the Longitudinal Valley, Taiwan.  
1003 *Tectonophysics*, 325, 43-62. doi:10.1016/S0040-1951(00)00130-X

1004 Chang, Y.H., Cheng, T.W., Lai, W.J., et al. (2012). Microbial methane cycling in a  
1005 terrestrial mud volcano in eastern Taiwan. *Environmental Microbiology*, 14,  
1006 895-908. doi:10.1111/j.1462-2920.2011.02658.x

1007 Chao, H.C., Pi, J.L., You, C.F., et al. (2021). Hydrogeology constrained by  
1008 multi-isotopes and volatiles geochemistry of hot springs in Tatun Volcanic Group,  
1009 Taiwan. *Journal of Hydrology*, 600, 126515. doi: 10.1016/j.jhydrol.2021.126515

1010 Chao, H.C., You, C.F., & Sun, C.H. (2010). Gases in Taiwan mud volcanoes:  
1011 Chemical composition, methane carbon isotopes, and gas fluxes. *Applied*  
1012 *Geochemistry*, 25, 428-436. doi:10.1016/j.apgeochem.2009.12.009

1013 Chao, H.C., You, C.F., Wang, B.S., et al. (2011). Boron isotopic composition of mud  
1014 volcano fluids: Implications for fluid migration in shallow subduction  
1015 zones. *Earth and Planetary Science Letters*, 305, 32-44.

1016 doi:10.1016/j.epsl.2011.02.033

1017 Chasar, L., Chanton, J., Glaser, P.H., et al. (2000). Radiocarbon and stable carbon  
1018 isotopic evidence for transport and transformation of dissolved organic carbon,  
1019 dissolved inorganic carbon, and CH<sub>4</sub> in a northern Minnesota peatland. *Global*  
1020 *Biogeochemical Cycles*, 14, 1095-1108. doi:10.1029/1999GB001221

1021 Chen, A.T., Sano, Y., Byrne, T.B., et al. (2020). Helium Isotopic Signature of a Plate  
1022 Boundary Suture in an Active Arc–Continent Collision. *Earth and Space*  
1023 *Chemistry*, 4, 1237-1246. doi:10.1021/acsearthspacechem.0c00038

1024 Chen, N.C., Yang, T.F., Hong, W.L., et al. (2020). Discharge of deeply rooted fluids  
1025 from submarine mud volcanism in the Taiwan accretionary prism. *Scientific*  
1026 *reports*, 10, 381. doi:10.1038/s41598-019-57250-9

1027 Chen, N.C., Yang, T.F., Hong, W.L., et al. (2017). Production, consumption, and  
1028 migration of methane in accretionary prism of southwestern Taiwan. *Geochemistry,*  
1029 *Geophysics, Geosystems*, 18, 2970-2989. doi:10.1002/2017GC006798

1030 Chen, S.C., Hsu, S.K., Tsai, C.H., et al. (2010). Gas seepage, pockmarks and mud  
1031 volcanoes in the near shore of SW Taiwan. *Marine Geophysical Researches*, 31,  
1032 133-147. doi:10.1007/s11001-010-9097-6

1033 Chen, S.C., Hsu, S.K., Wang, Y., et al. (2014). Distribution and characters of the mud  
1034 diapirs and mud volcanoes off southwest Taiwan. *Journal of Asian Earth Sciences*,  
1035 92, 201-214. doi:10.1016/j.jseaes.2013.10.009

1036 Chen, W.S., Yen, I.C., Fengler, K.P., et al. (2007). Late Holocene paleoearthquake  
1037 activity in the middle part of the Longitudinal Valley fault, eastern Taiwan. *Earth*  
1038 *and Planetary Science Letters*, 264, 420-437. doi:10.1016/j.epsl.2007.09.043

1039 Chen, W.S. (2016). *An introduction to the geology of Taiwan* (in Chinese). Geological  
1040 Society Located in Taipei.

1041 Cheng, T.W., Chang, Y.H., Tang, S.L., et al. (2012). Metabolic stratification driven by  
1042 surface and subsurface interactions in a terrestrial mud volcano. *ISME J*, 6,  
1043 2280-2290. doi:10.1038/ismej.2012.61

1044 Chen, Y. W., Shyu, J. B. H., & Chang, C. P. (2015). Neotectonic characteristics along  
1045 the eastern flank of the Central Range in the active Taiwan orogen inferred from  
1046 fluvial channel morphology. *Tectonics*, 34, 2249-2270. doi:10.1002/2014TC00379

1047 Chi, W.C., & Reed, D.L. (2008). Evolution of shallow, crustal thermal structure from  
1048 subduction to collision: An example from Taiwan. *Geological Society of America*

1049 *Bulletin*, 120, 679-690. doi:10.1130/b26210.1

1050 Chung, S.L., Yang, T.F., Lee, C.Y., et al. (1995). The igneous provinciality in Taiwan:  
1051 consequence of continental rifting superimposed by Luzon and Ryukyu subduction  
1052 systems. *Journal of Southeast Asian Earth Sciences*, 11, 73-80.  
1053 doi:10.1016/0743-9547(94)00040-L

1054 Chyi, L.L., Chou, C.Y., Yang, F.T., et al. (2001). Continuous radon measurements in  
1055 faults and earthquake precursor pattern recognition. *Western Pacific Earth*  
1056 *Sciences*, 1, 227-246. Doi: Code not available

1057 Craig, H. (1961). Isotopic variations in meteoric waters. *Science*, 133, 1702-1703.  
1058 doi:10.1126/science.133.3465.1702

1059 Dadson, S. J., Hovius, N., Chen, H., et al. (2003). Links between erosion, runoff  
1060 variability and seismicity in the Taiwan orogen. *Nature*, 426, 648-651.  
1061 doi:10.1038/nature02150

1062 Douglas, P.M., Stolper, D.A., Eiler, J.M., et al. (2017). Methane clumped isotopes:  
1063 Progress and potential for a new isotopic tracer. *Organic Geochemistry*, 113,  
1064 262-282. doi:10.1016/j.orggeochem.2017.07.016

1065 Epstein, G.S., Bebout, G.E., Christenson, B.W., et al. (2021). Cycling of CO<sub>2</sub> and N<sub>2</sub>  
1066 along the Hikurangi subduction margin, New Zealand: An integrated geological,  
1067 theoretical, and isotopic approach. *Geochemistry, Geophysics, Geosystems*, 22,  
1068 e2021GC009650. doi:10.1029/2021GC009650

1069 Etiopé, G. (2009). Natural emissions of methane from geological seepage in Europe.  
1070 *Atmospheric Environment*, 43, 1430-1443. doi:10.1016/j.atmosenv.2008.03.014

1071 Etiopé, G., & Lollar, B. (2013). Abiotic methane on Earth. *Reviews of Geophysics*, 51.  
1072 doi:10.1002/rog.20011

1073 Fellin, M.G., Chen, C.Y., Willett, S.D., et al. (2017). Erosion rates across space and  
1074 timescales from a multi-proxy study of rivers of eastern Taiwan. *Global and*  
1075 *Planetary Change*, 157, 174-193. doi:10.1016/j.gloplacha.2017.07.012

1076 Fu, C.C., Lai, C.W., Yang, T.F., et al. (2021). An automatic system for continuous  
1077 monitoring and sampling of groundwater geochemistry in earthquake-prone  
1078 regions of SW Taiwan. *Frontiers in Earth Science*, 9.  
1079 doi:10.3389/feart.2021.635913

1080 Fiebig, J., Stefansson, A., Ricci, A., et al. (2019). Abiogenesis not required to explain  
1081 the origin of volcanic-hydrothermal hydrocarbons. *Geochemical Perspectives*

1082 *Letters*. 23-27. doi:10.7185/geochemlet.1920

1083 Giunta, T., Young, E.D., Warr, O., et al. (2019). Methane sources and sinks in  
1084 continental sedimentary systems: New insights from paired clumped  
1085 isotopologues  $^{13}\text{CH}_3\text{D}$  and  $^{12}\text{CH}_2\text{D}_2$ . *Geochimica et Cosmochimica Acta*, 245,  
1086 327-351. doi:10.1016/j.gca.2018.10.030

1087 Giunta, T., Labidi, J., Kohl, I. E., et al. (2021). Evidence for methane isotopic bond  
1088 re-ordering in gas reservoirs sourcing cold seeps from the Sea of Marmara. *Earth  
1089 and Planetary Science Letters*, 553, 116619. doi:10.1016/j.epsl.2020.116619

1090 Giunta, T., Young, E.D., Labidi, J., et al. (2022). Extreme methane clumped  
1091 isotopologue bio-signatures of aerobic and anaerobic methanotrophy: insights  
1092 from the Lake Pavin and the Black Sea sediments. *Geochimica et Cosmochimica  
1093 Acta*, 338, 34-53. doi:10.1016/j.gca.2022.09.034

1094 Head, I.M., Jones, D.M., & Larter, S.R. (2003). Biological activity in the deep  
1095 subsurface and the origin of heavy oil. *Nature*, 426, 344-352.  
1096 doi:10.1038/nature02134

1097 Horibe, Y., & Craig, H. (1995). DH fractionation in the system  
1098 methane-hydrogen-water. *Geochimica et Cosmochimica Acta*, 59, 5209-5217.  
1099 doi:10.1016/0016-7037(95)00391-6

1100 Horita, J., & Wesolowski, D.J. (1994). Liquid-vapor fractionation of oxygen and  
1101 hydrogen isotopes of water from the freezing to the critical temperature.  
1102 *Geochimica et Cosmochimica Acta*, 58, 3425-3437. doi:  
1103 10.1016/0016-7037(94)90096-5

1104 Huang, S.T., Yang, K.M., Hung, J.H., et al. (2004). Deformation Front Development  
1105 at the Northeast Margin of the Tainan Basin, Tainan–Kaohsiung Area, Taiwan.  
1106 *Marine Geophysical Researches*, 25, 139-156. doi:10.1007/s11001-005-0739-z

1107 Jautzy, J.J., Douglas, P.M., Xie, H., et al. (2021).  $\text{CH}_4$  isotopic ordering records  
1108 ultra-slow hydrocarbon biodegradation in the deep subsurface. *Earth and  
1109 Planetary Science Letters*, 562, 116841.

1110 Karakashev, D., Batstone, D.J., Trably, E., et al. (2006). Acetate oxidation is the  
1111 dominant methanogenic pathway from acetate in the absence of Methanosaetaceae.  
1112 *Applied and Environmental Microbiology*, 72, 5138-5141.  
1113 doi:10.1128/AEM.00489-06

1114 Klaucke, I., Berndt, C., Crutchley, G., et al. (2016). Fluid venting and seepage at

1115 accretionary ridges: the Four Way Closure Ridge offshore SW Taiwan.  
1116 *Geo-Marine Letters*, 36, 165-174. doi:10.1007/s00367-015-0431-5

1117 Kietäväinen, R., & Purkamo, L. (2015). The origin, source, and cycling of methane in  
1118 deep crystalline rock biosphere. *Frontiers in Microbiology*, 6, 725.  
1119 doi:10.3389/fmicb.2015.00725

1120 Kopf, A.J. (2003). Global methane emission through mud volcanoes and its past and  
1121 present impact on the Earth's climate. *International Journal of Earth Sciences*, 92,  
1122 806-816. doi:10.1007/s00531-003-0341-z

1123 Krause, S.J., Liu, J., Young, E.D., & Treude, T. (2022).  $\Delta^{13}\text{CH}_3\text{D}$  and  $\Delta^{12}\text{CH}_2\text{D}_2$   
1124 signatures of methane aerobically oxidized by *Methylosinus trichosporium* with  
1125 implications for deciphering the provenance of methane gases. *Earth and*  
1126 *Planetary Science Letters*, 593, 117681. doi:10.1016/j.epsl.2022.117681

1127 Kunath, P., Chi, W.C., Berndt, C., et al. (2020). A shallow seabed dynamic gas hydrate  
1128 system off SW Taiwan: Results from 3-D seismic, thermal, and fluid migration  
1129 analyses. *Journal of Geophysical Research: Solid Earth*, 125, e2019JB019245-T.  
1130 doi:10.1029/2019JB019245

1131 Kunath, P., Crutchley, G., Chi, W.C., et al. (2022). Episodic venting of a submarine  
1132 gas seep on geological time scales: Formosa Ridge, northern South China Sea.  
1133 *Journal of Geophysical Research: Solid Earth*, 127, e2022JB024668.  
1134 doi:10.1029/2022JB024668

1135 Labidi, J., & Young, E. (2022). The origin and dynamics of nitrogen in the Earth's  
1136 mantle constrained by  $^{15}\text{N}^{15}\text{N}$  in hydrothermal gases. *Chemical Geology*, 591,  
1137 120709. doi:10.1016/j.chemgeo.2022.120709

1138 Labidi, J., Young, E.D., Giunta, T., et al. (2020). Methane thermometry in deep-sea  
1139 hydrothermal systems: Evidence for re-ordering of doubly-substituted  
1140 isotopologues during fluid cooling. *Geochimica et Cosmochimica Acta*, 288,  
1141 248-261. doi:10.1016/j.gca.2020.08.013

1142 Labidi, J., Young, E.D., Fischer, T.P., et al. (2021). Recycling of nitrogen and light  
1143 noble gases in the Central American subduction zone: Constraints from  $^{15}\text{N}^{15}\text{N}$ .  
1144 *Earth and Planetary Science Letters*, 571, 117112. doi:10.1016/j.epsl.2021.117112

1145 Lacombe, O., Mouthereau, F., Deffontaines, B., et al. (1999). Geometry and  
1146 Quaternary kinematics of fold-and-thrust units of southwestern Taiwan. *Tectonics*,

1147 18, 1198-1223. doi:10.1029/1999TC900036

1148 Lallemand, S. (2016). Philippine Sea Plate inception, evolution, and consumption  
1149 with special emphasis on the early stages of Izu-Bonin-Mariana subduction.  
1150 *Progress in Earth and Planetary Science*, 3, 15. doi:10.1186/s40645-016-0085-6

1151 Lai, L.S.H., Roering, J.J., Finnegan, N.J., et al. (2021). Coarse sediment supply sets  
1152 the slope of bedrock channels in rapidly uplifting terrain: Field and topographic  
1153 evidence from eastern Taiwan. *Earth Surface Processes and Landforms*, 46,  
1154 2671-2589. doi:10.1002/esp.5200

1155 Lee, Y.H., Byrne, T.B., Lo, W., et al. (2022). Out of sequence faulting in the  
1156 backbone range, Taiwan: Implications for thickening and exhumation processes.  
1157 *Earth and Planetary Science Letters*, 594, 117711.  
1158 doi:10.1016/j.epsl.2022.117711

1159 Lin, A.T., Liu, C.S., Lin, C.C., et al. (2008). Tectonic features associated with the  
1160 overriding of an accretionary wedge on top of a rifted continental margin: An  
1161 example from Taiwan. *Marine Geology*, 255, 186-203.  
1162 doi:10.1016/j.margeo.2008.10.002

1163 Lin, Y.T., Tu, T.H., Wei, C.L., et al. (2018). Steep redox gradient and biogeochemical  
1164 cycling driven by deeply sourced fluids and gases in a terrestrial mud volcano.  
1165 *FEMS Microbiology Ecology*, 94, 3796. doi:10.1093/femsec/fiy171

1166 Lin, Y.T., Rumble, D., Young, E., Labidi, J., Tu, T.H., Chen, J.N. Pape, T., Bohrmann,  
1167 G., Lin, S., Lin, L.H., and Wang, P.L. (2023). Supplementary Information for  
1168 “Diverse origins of gases from mud volcanoes and seeps in tectonically  
1169 fragmented terrane” [Dataset]. Zenodo. doi: 10.5281/zenodo.8275042.

1170 Ling, Y.C., Chen, Y.J., Sun, C.H., et al. (2012). Potential of microbial methane  
1171 formation in a high-temperature hydrocarbon seep. *Applied Geochemistry*, 27,  
1172 1666-1678. doi:10.1016/j.apgeochem.2012.04.002

1173 Liu, J., Harris, R.L., Ash, J.L., et al. (2023). Reversibility controls on extreme  
1174 methane clumped isotope signatures from anaerobic oxidation of methane.  
1175 *Geochimica et Cosmochimica Acta*, 348, 165-186. doi:10.1016/j.gca.2023.02.022

1176 Liu, C.S., Huang, I.L., & Teng, L.S. (1997). Structural features off southwestern  
1177 Taiwan. *Marine Geology*, 137, 305-319. doi:10.1016/S0025-3227(96)00093-X

1178 Lundegard, P.D., Sweeney, R.E., & Ririe, G.T. (2000). Soil gas methane at petroleum  
1179 contaminated sites: Forensic determination of origin and source. *Environmental*

1180 *forensics*, 1, 3-10. doi:10.1006/enfo.1998.0002

1181 Lu, Y.C., Song, S. R., Lin, P. H., et al. (2020). Thermal Fluid Changes after Operating  
1182 a Geothermal System: A Case Study of the Chingshui Geothermal Field, Taiwan.  
1183 *Geothermics*, 87, 101878. doi: 10.1016/j.geothermics.2020.101878

1184 Mazzini, A., & Etiope, G. (2017). Mud volcanism: An updated review. *Earth-Science*  
1185 *Reviews*, 168, 81-112. doi:10.1016/j.earscirev.2017.03.001

1186 Milkov, A.V. (2011). Worldwide distribution and significance of secondary microbial  
1187 methane formed during petroleum biodegradation in conventional reservoirs.  
1188 *Organic Geochemistry*, 42, 184-207. doi:10.1016/j.orggeochem.2010.12.003

1189 Milkov, A.V., & Etiope, G. (2018). Revised genetic diagrams for natural gases based  
1190 on a global dataset of >20,000 samples. *Organic Geochemistry*, 125, 109-120.  
1191 doi:10.1016/j.orggeochem.2018.09.002

1192 Mishima, K., Sumino, H., Yamada, T., et al. (2018). Accurate determination of the  
1193 absolute  $^3\text{He}/^4\text{He}$  ratio of a synthesized helium standard gas (Helium Standard of  
1194 Japan, HESJ): toward revision of the atmospheric  $^3\text{He}/^4\text{He}$  ratio. *Geochemistry,*  
1195 *Geophysics, Geosystems*, 19, 3995-4005. doi:10.1029/2018GC007554

1196 Ono, S., Rhim, J.H., Gruen, D.S., Taubner, H., et al. (2021). Clumped isotopologue  
1197 fractionation by microbial cultures performing the anaerobic oxidation of methane.  
1198 *Geochimica et Cosmochimica Acta*, 293, 70-85. doi:10.1016/j.gca.2020.10.015

1199 Ono, S., Rhim, J.H., & Ryberg, E.C. (2022). Rate limits and isotopologue  
1200 fractionations for microbial methanogenesis examined with combined pathway  
1201 protein cost and isotopologue flow network models. *Geochimica et Cosmochimica*  
1202 *Acta*. doi:10.1016/j.gca.2022.03.017

1203 Ono, S., Wang, D.T., Gruen, D.S., et al. (2014). Measurement of a doubly substituted  
1204 methane isotopologue,  $^{13}\text{CH}_3\text{D}$ , by tunable infrared laser direct absorption  
1205 spectroscopy. *Analytical Chemistry*, 86, 6487-6494. doi:10.1021/ac5010579

1206 Pape, T., Hohnberg, H.J., Wunsch, D., et al. (2017). Design and deployment of  
1207 autoclave pressure vessels for the portable deep-sea drill rig MeBo  
1208 (Meeresboden-Bohrgerät). *Scientific Drilling*, 23, 29-37.  
1209 doi:10.5194/sd-23-29-2017

1210 Pepper, A.S., & Corvi, P.J. (1995). Simple kinetic models of petroleum formation.  
1211 Part I: oil and gas generation from kerogen. *Marine and Petroleum Geology*, 12,  
1212 291-319. doi:10.1016/0264-8172(95)98381-E

1213 Peng, T.R., Wang, C.H., Huang, C.C., et al. (2010). Stable isotopic characteristic of  
1214 Taiwan's precipitation: A case study of western Pacific monsoon region. *Earth and*  
1215 *Planetary Science Letters*, 289, 357-366. doi:10.1016/j.epsl.2009.11.024

1216 Poreda, R., & Craig, H. (1989). Helium isotope ratios in circum-Pacific volcanic arcs.  
1217 *Nature*, 338, 473-478. doi:10.1038/338473a0

1218 Rau, R.J., Lee, J.C., Ching, K.E., et al. (2012). Subduction-continent collision in  
1219 southwestern Taiwan and the 2010 Jiashian earthquake sequence. *Tectonophysics*,  
1220 578, 107-116. doi:10.1016/j.tecto.2011.09.013

1221 Roulleau, E., Sano, Y., Takahata, N., et al. (2015). He, Ar, N and C isotope  
1222 compositions in Tatun Volcanic Group (TVG), Taiwan: Evidence for an important  
1223 contribution of pelagic carbonates in the magmatic source. *Journal of Volcanology*  
1224 *and Geothermal Research*, 303, 7-15. doi:10.1016/j.jvolgeores.2015.07.017

1225 Rumble, D., Ash, J.L., Wang, P.L., et al. (2018). Resolved measurements of <sup>13</sup>CDH<sub>3</sub>  
1226 and <sup>12</sup>CD<sub>2</sub>H<sub>2</sub> from a mud volcano in Taiwan. *Journal of Asian Earth Sciences*, 167,  
1227 218-221. doi:10.1016/j.jseaes.2018.03.007

1228 Sano, Y., Kinoshita, N., Kagoshima, T., et al. (2017). Origin of methane-rich natural  
1229 gas at the West Pacific convergent plate boundary. *Scientific reports*, 7, 1-10.  
1230 doi:10.1038/s41598-017-15959-5

1231 Sano, Y., Tokutake, T., & Takahata, N. (2008). Accurate measurement of atmospheric  
1232 helium isotopes. *Analytical sciences: The international journal of the Japan*  
1233 *Society for Analytical Chemistry*, 24, 521-525. doi:10.2116/analsci.24.521

1234 Schoell, M. (1988). Multiple origins of methane in the Earth. *Chemical Geology*, 71,  
1235 1-10. doi:10.1016/0009-2541(88)90101-5

1236 Scholten, J.C., & Conrad, R. (2000). Energetics of syntrophic propionate oxidation in  
1237 defined batch and chemostat cocultures. *Applied and Environmental Microbiology*,  
1238 66, 2934-2942. doi:10.1128/AEM.66.7.2934-2942.2000

1239 Shao, W.Y., Chung, S.L., & Chen, W.S. (2014). Zircon U-Pb Age Determination of  
1240 Volcanic Eruptions in Lutao and Lanyu in the Northern Luzon Magmatic Arc.  
1241 *Terrestrial, Atmospheric and Oceanic Sciences*, 25, 149.  
1242 doi:10.3319/TAO.2013.11.06.01(TT)

1243 Shuai, Y., Douglas, P.M., Zhang, S., et al. (2018). Equilibrium and non-equilibrium  
1244 controls on the abundances of clumped isotopologues of methane during  
1245 thermogenic formation in laboratory experiments: implications for the chemistry

1246 of pyrolysis and the origins of natural gases. *Geochimica et Cosmochimica Acta*,  
1247 223, 159-174. doi:10.1016/j.gca.2017.11.024

1248 Stolper, D.A., Lawson, M., Davis, C.L., et al. (2014). Formation temperatures of  
1249 thermogenic and biogenic methane. *Science*, 344, 1500-1503, doi:  
1250 10.1126/science.1254509

1251 Stolper, D.A., Martini, A.M., Clog, M., et al. (2015). Distinguishing and  
1252 understanding thermogenic and biogenic sources of methane using multiply  
1253 substituted isotopologues. *Geochimica et Cosmochimica Acta*, 161, 219-247.  
1254 doi:10.1016/j.gca.2015.04.015

1255 Summons, R.E., Franzmann, P.D., & Nichols, P.D. (1998). Carbon isotopic  
1256 fractionation associated with methylotrophic methanogenesis. *Organic  
1257 Geochemistry*, 28, 465-475. doi:10.1016/S0146-6380(98)00011-4

1258 Sun, C.H., Chang, S.C., Kuo, C.L., et al. (2010). Origins of Taiwan's mud volcanoes:  
1259 Evidence from geochemistry. *Journal of Asian Earth Sciences*, 37, 105-116.  
1260 doi:10.1016/j.jseaes.2009.02.007

1261 Suppe, J. (1984). Kinematics of arc-continent collision, flipping of subduction, and  
1262 back-arc spreading near Taiwan. *Geological Society of China Memoir*, 6, 131-146

1263 Takai, K., Nakamura, K., Toki, T., et al. (2008). Cell proliferation at 122°C and  
1264 isotopically heavy CH<sub>4</sub> production by a hyperthermophilic methanogen under  
1265 high-pressure cultivation. *Proceedings of the National Academy of Sciences*, 105,  
1266 10949-10954. doi:10.1073/pnas.0712334105

1267 Teng, L.S., & Lin, A.T. (2004). Cenozoic tectonics of the China continental margin:  
1268 Insights from Taiwan. *Geological Society, London, Special Publications*, 226,  
1269 313-332. doi:10.1144/gsl.Sp.2004.226.01.17

1270 Tseng, Y., Römer, M., Lin, S., et al. (2023). Yam Seep at Four-Way Closure Ridge: a  
1271 prominent active gas seep system at the accretionary wedge SW offshore Taiwan.  
1272 *International Journal of Earth Sciences*, 112, 1043-1061.  
1273 doi:10.1007/s00531-022-02280-4

1274 Warr, O., Young, E. D., Giunta, T., et al. (2021). High-resolution, long-term isotopic  
1275 and isotopologue variation identifies the sources and sinks of methane in a deep  
1276 subsurface carbon cycle. *Geochimica et Cosmochimica Acta*, 294, 315-334.  
1277 doi:10.1016/j.gca.2020.12.002

1278 Wang, D.T., Gruen, D.S., Lollar, B.S., et al. (2015). Nonequilibrium clumped isotope

1279 signals in microbial methane. *Science*, 348, 428. doi:10.1126/science.aaa4326

1280 Wang, P.-L., Wu, J.-J., Yeh, E.-C., et al. (2010) Isotopic constraints of vein carbonates  
1281 on fluid sources and processes associated with the ongoing brittle deformation  
1282 within the accretionary wedge of Taiwan. *Terra Nova*, 22, 251–256. doi:  
1283 10.1111/j.1365-3121.2010.00940.x

1284 Wang, P.L., Chiu, Y.P., Cheng, T.W., et al. (2014). Spatial variations of community  
1285 structures and methane cycling across a transect of Lei-Gong-Hou mud volcanoes  
1286 in eastern Taiwan. *Frontiers in Microbiology*, 5, 121. doi:10.3389/fmicb.2014.001

1287 Wang, Y., Lin, Y.N., Ota, Y., et al. (2022). Mud Diapir or Fault-Related Fold? On the  
1288 Development of an Active Mud-Cored Anticline Offshore Southwestern Taiwan.  
1289 *Tectonics*, 41, e2022TC007234. doi:10.1029/2022TC007234

1290 Whiticar, M.J. (1999). Carbon and hydrogen isotope systematics of bacterial  
1291 formation and oxidation of methane. *Chemical Geology*, 161, 291-314.  
1292 doi:10.1016/S0009-2541(99)00092-3

1293 Xia, X., & Gao, Y. (2019). Kinetic clumped isotope fractionation during the thermal  
1294 generation and hydrogen exchange of methane. *Geochimica et Cosmochimica*  
1295 *Acta*, 248, 252-273. doi:10.1016/j.gca.2019.01.004

1296 Xia, X., & Gao, Y. (2021). Methane from microbial hydrogenolysis of sediment  
1297 organic matter before the great oxidation event. *Nature communications*, 12, 5032.  
1298 doi:10.1038/s41467-021-25336-6

1299 Yang, T.F., Chen, C.H., Tien, R.L., et al. (2003). Remnant magmatic activity in the  
1300 Coastal Range of East Taiwan after arc–continent collision: fission-track data and  
1301  $^3\text{He}/^4\text{He}$  ratio evidence. *Radiation Measurements*, 36, 343-349.  
1302 doi:10.1016/S1350-4487(03)00149-5

1303 Yang, T.F., Yeh, G.H., Fu, C.C., et al. (2004). Composition and exhalation flux of  
1304 gases from mud volcanoes in Taiwan. *Environmental Geology*, 46, 1003-1011.  
1305 doi:10.1007/s00254-004-1086-0

1306 Yeh, Y.L., Strong, W., Chien W.C., et al. (2016). Tomography of the Chukou Fault  
1307 zone, southwest Taiwan: Insights from microearthquake data. *TAO: Terrestrial,*  
1308 *Atmospheric and Oceanic Sciences*, 27, 387. doi:10.3319/TAO.2016.01.29.01

1309 Yen, J.Y., Chen, K.S., Chang, C.P., et al. (2008). Evaluation of earthquake potential  
1310 and surface deformation by differential interferometry. *Remote Sensing of*  
1311 *Environment*, 112, 782-795. doi:10.1016/j.rse.2007.06.012

- 1312 Yeung, L.Y., Li, S., Kohl, I.E., et al. (2017). Extreme enrichment in atmospheric  
1313  $^{15}\text{N}^{15}\text{N}$ . *Science Advances*, 3, 6741. doi:10.1016/j.chemgeo.2022.120709
- 1314 You, C.F., Gieskes, J. M., Lee, T., et al. (2004). Geochemistry of mud volcano fluids  
1315 in the Taiwan accretionary prism. *Applied Geochemistry*, 19, 695-707.  
1316 doi:10.1016/j.apgeochem.2003.10.004
- 1317 Young, E.D., Kohl, I.E., Lollar, B.S., et al. (2017). The relative abundances of  
1318 resolved  $^{12}\text{CH}_2\text{D}_2$  and  $^{13}\text{CH}_3\text{D}$  and mechanisms controlling isotopic bond ordering  
1319 in abiotic and biotic methane gases. *Geochimica et Cosmochimica Acta*, 203,  
1320 235-264. doi:10.1016/j.gca.2016.12.041
- 1321 Young, E.D., Rumble, D., Freedman, P., et al. (2016). A large-radius  
1322 high-mass-resolution multiple-collector isotope ratio mass spectrometer for  
1323 analysis of rare isotopologues of  $\text{O}_2$ ,  $\text{N}_2$ ,  $\text{CH}_4$  and other gases. *International*  
1324 *Journal of Mass Spectrometry*, 401, 1-10. doi:10.1016/j.ijms.2016.01.006
- 1325 Yu, H.S., & Chang, E. T. Y. (2009). Links among slope morphology, canyon types and  
1326 tectonics on passive and active margins in the northernmost South China Sea.  
1327 *Journal of Earth Science*, 20, 77-84. doi:10.1007/s12583-009-0008

1328

1329 *Figure captions*

1330 Figure 1. Isotopic and abundance characteristics of hydrocarbons and  $\text{CO}_2$  for  
1331 analyzed samples. (a)  $\delta^{13}\text{C}_{\text{CH}_4}$  versus  $\delta^2\text{H}_{\text{CH}_4}$  values (data from Table S2); (b)  
1332  $\text{C}_1/(\text{C}_2+\text{C}_3)$  ratios versus  $\delta^{13}\text{C}_{\text{CH}_4}$  values (data from Table S1); (c)  $\delta^{13}\text{C}_{\text{CO}_2}$   
1333 versus  $\delta^{13}\text{C}_{\text{CH}_4}$  values (data from Table S1). The plotted fields are divided into  
1334 areas for “primary microbial” (shaded in green and blue), “secondary microbial”  
1335 (encircled by dashed lines and abbreviated as “SM”), “thermogenic” (shaded in  
1336 yellow), and “abiotic” (shaded in orange) formation processes following the  
1337 ranges of Milkov and Etiope (2018). “Primary microbial” methane is further  
1338 divided into two categories, with “F” for the fermentation of methylated  
1339 compounds, and “CR” for the  $\text{CO}_2$  reduction. Results are categorized by  
1340 structural domains (yellow squares – Chukou Fault, green circles – Chishan  
1341 Fault, crosses – Guitingkeng Anticline, light yellow circles – Coastal Plain, blue  
1342 squares – offshore FR and FWCR sites, orange triangles – Coastal Range).  
1343 Green and black arrows in (a) and (b) show the possible trends for microbial  
1344 methane oxidation and diffusion of migratory methane, respectively. The slope

1345 of the arrow does not indicate the precise variation trend. Some published  
1346 results for different processes simultaneously characterized by the abundances  
1347 of doubly substituted isotopologues (Young et al., 2017; Giunta et al., 2019) are  
1348 plotted for comparison.

1349

1350 Figure 2.  $\Delta^{12}\text{CH}_2\text{D}_2$  versus  $\Delta^{13}\text{CH}_3\text{D}$  values for analyzed samples. The equilibrium  
1351 curve marked with temperature was calculated following Young et al. (2016).  
1352 Sample legends are the same as those in Figure 1. Values for microbial methane  
1353 produced from methylated compounds and from  $\text{CO}_2$  in the lab (blue diamonds  
1354 encompassed with an arbitrarily defined range in green and gray; Young et al.,  
1355 2017 and Giunta et al., 2019), abiotic methane produced in the laboratory  
1356 (orange diamonds) or recovered from the field (gray circles with cross marks)  
1357 (Young et al., 2017) are plotted for comparison. Green, black, and blue arrows  
1358 show the possible trends for aerobic oxidation of methane, diffusion of  
1359 migratory methane, and anaerobic oxidation of methane (AOM), respectively.  
1360 The slope of the arrow does not indicate the precise variation trend. Data  
1361 distribution within the region encircled by a dashed rectangle is enlarged in the  
1362 lower right corner.

1363

1364 Figure 3.  $^{20}\text{Ne}/^4\text{He}$  versus  $^3\text{He}/^4\text{He}$  ratios (in Ra) for analyzed samples. A three  
1365 end-component mixing model encompasses “crust”, “mantle”, and “air”  
1366 components with He isotope ratios of 0.01, 8, and 1 Ra, respectively (Poreda &  
1367 Craig, 1989). Legends are the same as those in Figure 1.

1368

1369 Figure 4. Water isotopic compositions and fractionations, and methane isotopologue  
1370 abundances. (a) Water  $\delta^2\text{H}$  versus  $\delta^{18}\text{O}$  values for analyzed samples. Legends  
1371 are the same as those in Figure 1 (except for the red star for seawater from the  
1372 Green Island; small blue circles for meteoric water in eastern and southern  
1373 Taiwan). The solid line indicates the global meteoric water line (GMWL; Craig,  
1374 1961), whereas the dashed line is the local meteoric water line (LMWL; Peng et  
1375 al., 2010). The dotted lines with arrows indicate the potential mixing between  
1376 deeply sourced water and meteoric water or seawater. Data for mud volcanoes  
1377 published in previous studies are also plotted for comparison. (b)  $\Delta^{13}\text{CH}_3\text{D}$  and  
1378 (c)  $\Delta^{12}\text{CH}_2\text{D}_2$  values versus hydrogen isotopic fractionations ( $\epsilon$ ; defined as  
1379  $(\alpha-1)\times 1000\text{‰}$ , where  $\alpha$  is the fractionation factor (eq. 8) between methane and  
1380 water). The equilibrium curves (in blue dashed lines) are plotted using the  
1381 relationships described in Horita & Wesolowski (1994) and Horibe & Craig

1382 (1995). The dotted lines indicate an infinite temperature that is based on two  
1383 methane isotopologue abundances (Young et al., 2016).

1384

1385 Figure 5. Schematic geological cross sections (modified from Chen (2016)) overlaid  
1386 with the estimated depths of methane formation (solid orange circles) based on  
1387 methane isotopologue abundances (this study) and local geothermal gradients  
1388 (Chi & Reed, 2008) (Table S6). The geographic distribution of each cross  
1389 section is excerpted from the solid lines in Figure 5d. Faults with the shearing  
1390 sense related to individual structural domains were shown in black dashed lines  
1391 with arrows. The estimated depths of methane formation are projected directly  
1392 on the related faults to help visualize the possible two-dimensional range where  
1393 methane is formed. Therefore, it is likely that the exact positions of methane  
1394 formation deviate from the attributed fault systems (e.g., blind faults).  
1395 Interpretations for the origins of methane and helium are also provided in  
1396 parentheses next to site names with the first letter denoting for methane (T for  
1397 thermogenic, B for biogenic, and A for abiotic) and the second letter for helium  
1398 (C for crust and M for mantle). Although the temperature (and depth) estimate  
1399 (~190°C) based on two methane isotopologue abundances for site WD is  
1400 available, no schematic cross section has been published due to the lack of  
1401 subsurface geology data.

1402

Figure 1.

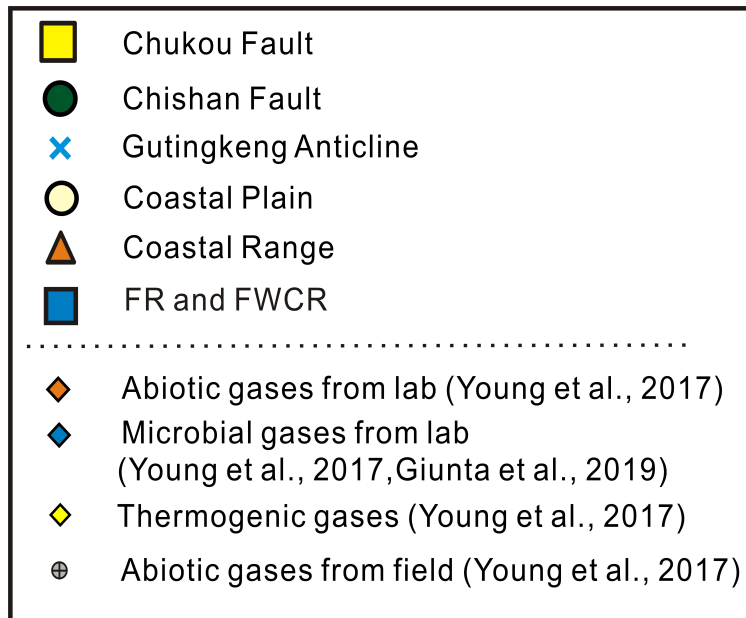
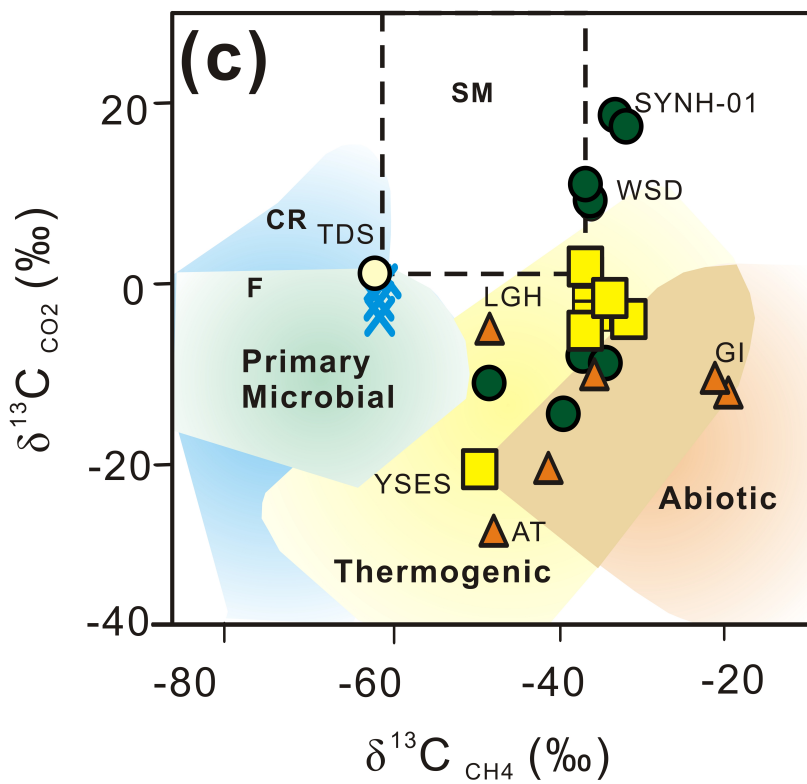
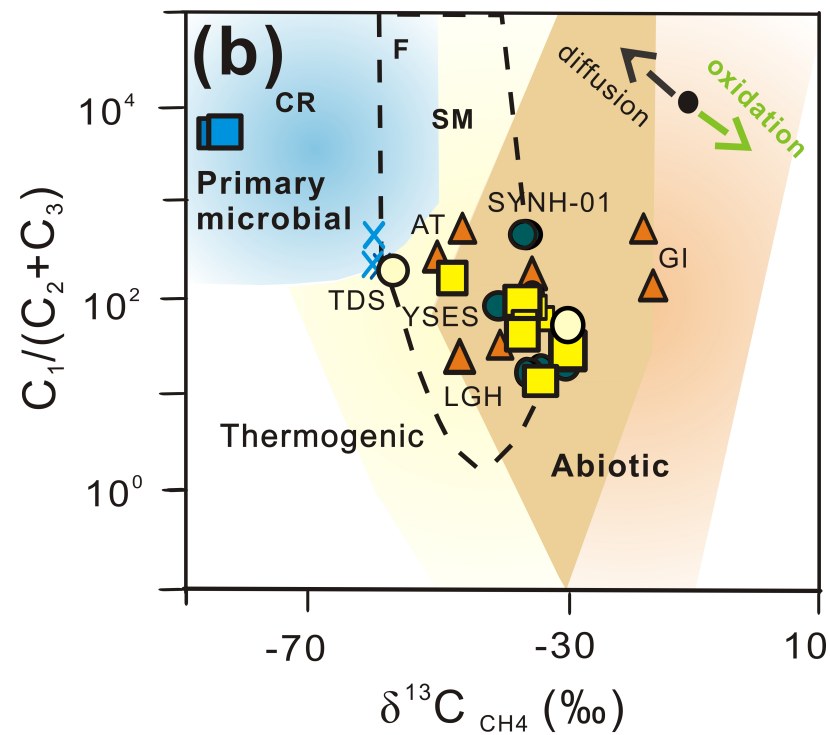
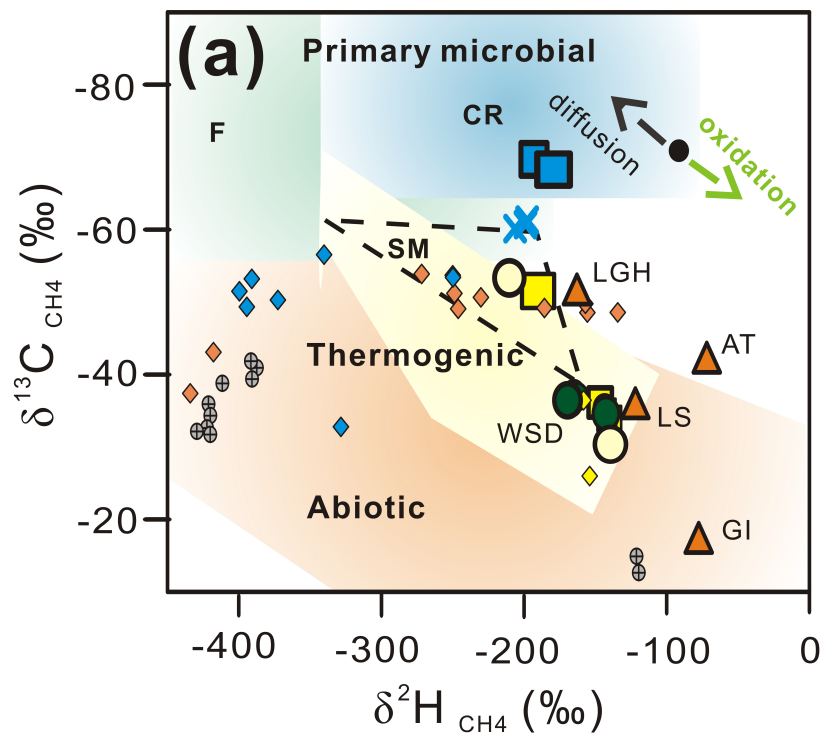


Figure 2.

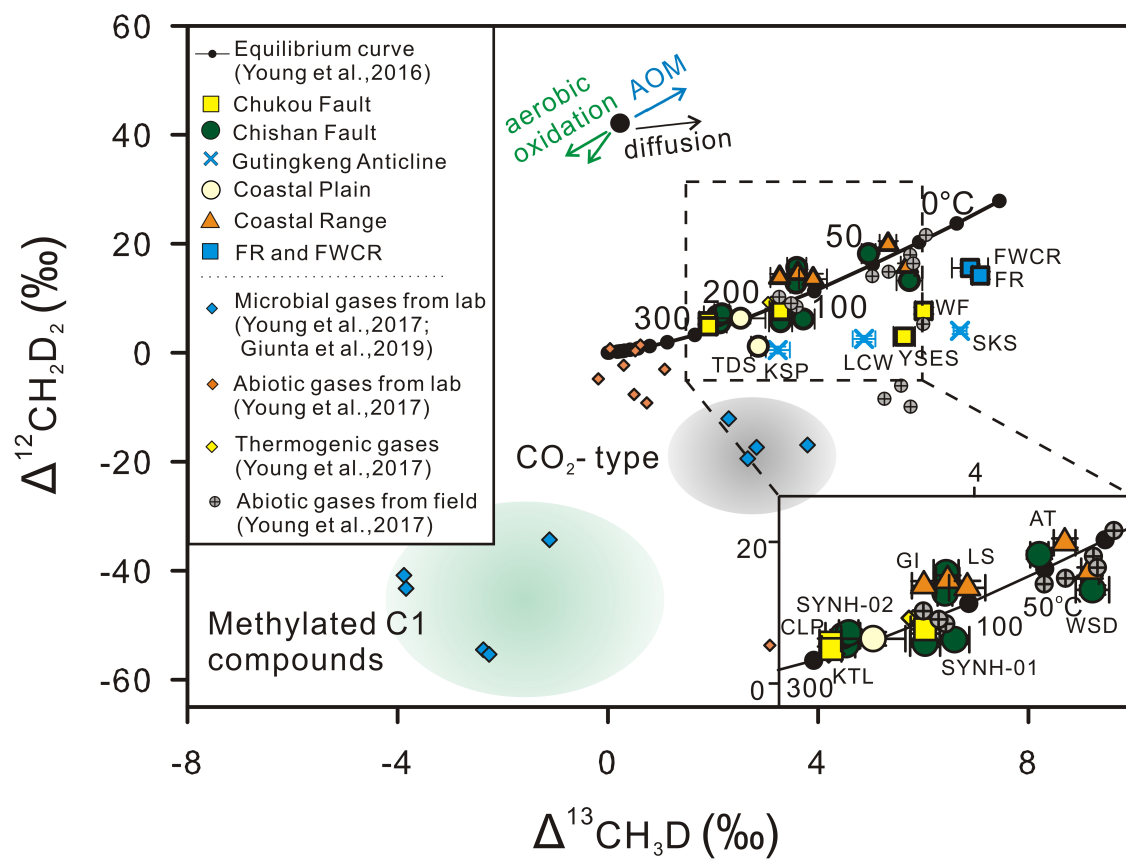


Figure 3.

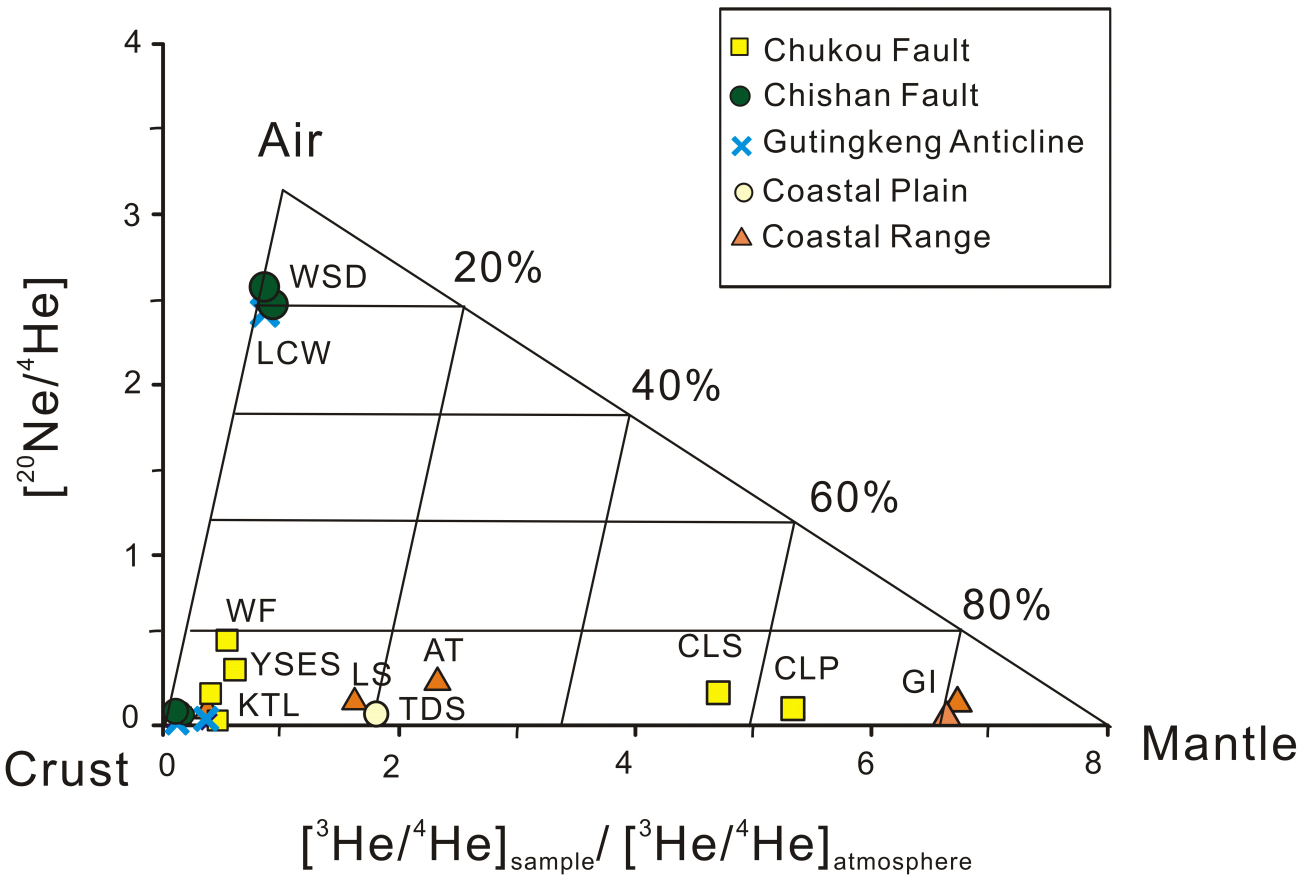


Figure 4.

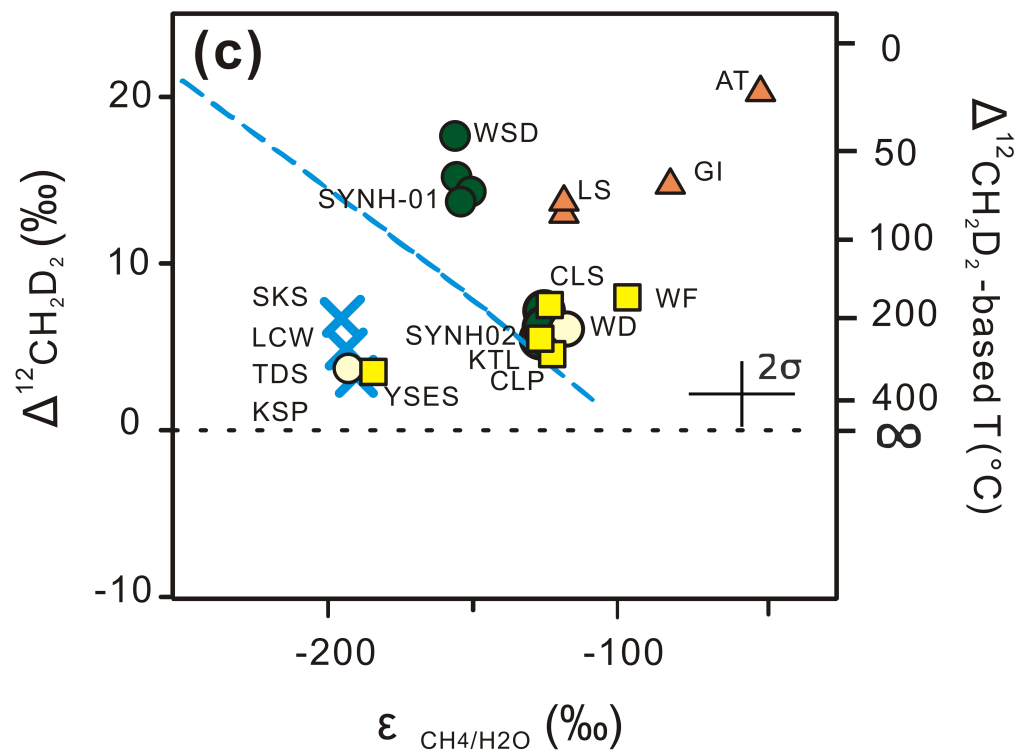
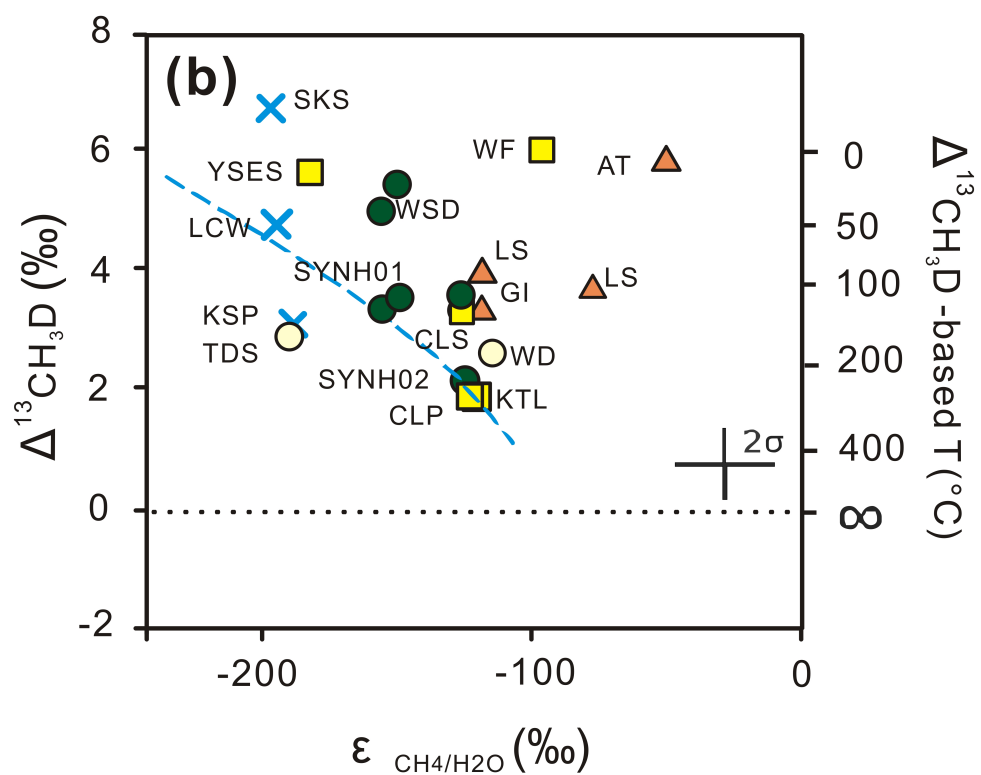
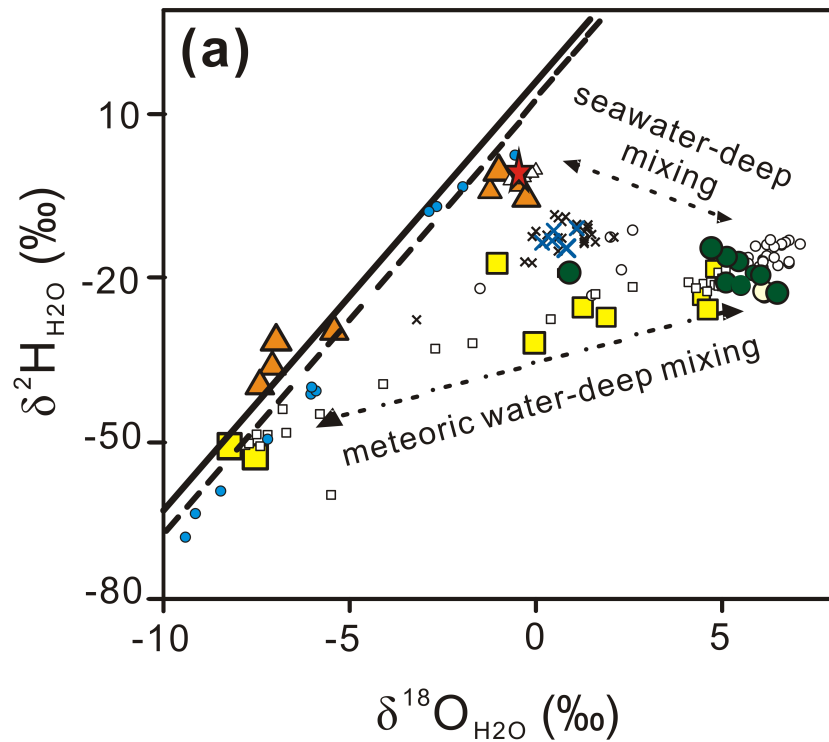


Figure 5.

